

Growth and Properties of BiMnO₃ Thin Films

Kuan-Cheng Yeh

A Thesis Submitted in Fulfillment of the Requirements for the Degree of Master of
Philosophy of Imperial College London

Department of Materials

Imperial College London

2013

Copyright Declaration

The copyright of this thesis rests with the author and is made available under a Creative Commons Attribution Non-Commercial No Derivatives licence. Researchers are free to copy, distribute or transmit the thesis on the condition that they attribute it, that they do not use it for commercial purposes and that they do not alter, transform or build upon it. For any reuse or redistribution, researchers must make clear to others the licence terms of this work

Declaration of Originality

I, Kuan-Cheng Yeh, declare that the work presented in this thesis is my own and any references to other works and contribution from other persons or groups are appropriately cited through the thesis.

Abstract

BiMnO₃ thin films were epitaxially grown on SrTiO₃ (100) substrates using pulsed laser deposition (PLD). The growth of thin films was extremely sensitive to substrate deposition temperatures, and single-phase BiMnO₃ only could be formed in a narrow temperature window of around 640°C in an oxygen pressure of 75mTorr. It was found that the post annealing at 550°C in an oxygen pressure of 7.6×10^5 mTorr effectively improved the crystallinity of the film. The BiMnO₃ films were found to be strongly (-202) oriented. The out-of-plane orientation relationship was (-202) BiMnO₃ || (100) SrTiO₃. From the result of phi (ϕ) scan, the (-202) plane showed a four-fold rotational symmetry, and the existence of a 45° rotation between the SrTiO₃ (100) plane and the BiMnO₃ (-202) plane. Magnetic measurements revealed that the BiMnO₃ thin film was ferromagnetic with a Curie temperature (T_c) of about 80K, lower than that of the bulk material.

Acknowledgements

This work is a collaborative effort. Without the help and participation of many talented and generous people at Imperial College London, this work would not have been possible. I would like to thank those who have helped during the course of writing this thesis.

First and foremost, I would like to express my sincere thanks to Dr Yeong-Ah Soh who gave me the opportunity to work on this project and generously provided many advices on my research. My deep gratitude and thanks go to my supervisor, Dr Martyn A McLachlan; his guidance, expertise, and patience were essential during this research process. My continued gratitude goes to my co-supervisor, Dr Peter K Petrov, for his assistance and expertise.

My sincere appreciation goes to Dr Stephen Skinner for his permission for me to use the furnaces. Big thanks go to Mr Richard Sweeney for his generous assistance in the course of XRD, and to Dr Mahmoud Ardakani for his support and assistance on my SEM work. A special thank you to Dr Ullrich Hannemann for his help on the PPMS measurement. My appreciation and gratitude go to Dr Bin Zhou and Mr Kuan-Ting Wu for their assistance on the training of pulsed laser deposition equipment. It has been a privilege to work with all of you!

Finally, I thank God for the opportunity to accomplish this thesis and keep my health off a difficult situation. I also gratefully acknowledge the love and support of all my family members and friends.

Table of Contents

Copyright Declaration.....	2
Declaration of Originality.....	3
Abstract.....	4
Acknowledgements.....	5
Table of Contents.....	6
List of Figures.....	9
List of Tables.....	14
Chapter1 Introduction.....	15
1.1 Multiferroic Materials.....	15
1.1.1 Single Phase Multiferroic Materials.....	16
1.1.2 Composite Multiferroic Materials.....	19
1.2 Possible Applications of Multiferroic Materials.....	21
1.2.1 Memory Devices.....	21
1.2.1.1 Memory Devices Based on Exchange Bias.....	21
1.2.1.2 Memory Devices Based On Tunneling Magnetoresistance	24
1.2.2 Magnetic Field Sensors.....	26
1.3 Bismuth Manganite (BiMnO ₃).....	27
1.3.1 Ferromagnetism of BiMnO ₃	30
1.3.2 Ferroelectricity of BiMnO ₃	34
1.3.3 Magnetoelectric Coupling of BiMnO ₃	35
1.3.4 Electronic Properties of BiMnO ₃	36
1.4 Modes of Film Growth by Vapor Deposition.....	37
1.4.1 Domain Matching Epitaxy (DME).....	39
1.5 Research Problems.....	41

Chapter2	Experimental Techniques.....	42
2.1	Pulsed Laser Deposition (PLD) of Thin Films.....	42
	2.1.1 The Effect of Laser Fluence.....	45
	2.1.2 The Effect of Background Gas.....	45
	2.1.3 The Effect of Target-Substrate Separation.....	45
	2.1.4 The Effect of Growth Temperatures.....	46
2.2	Preparation of PLD Targets of BiMnO ₃	46
2.3	X-ray Diffraction (XRD).....	46
2.4	Scanning Electron Microscopy (SEM).....	51
2.5	Density Measurement of PLD Targets.....	53
2.6	Thickness Measurement of Thin Films.....	54
2.7	Magnetic Measurement by PPMS.....	55
Chapter 3	Result and Discussion.....	59
3.1	Characterization of Bi _{1.2} MnO ₃ Target.....	59
	3.1.1 Qualitative Compositional Analysis.....	59
	3.1.2 Density Determination.....	61
3.2	Thin Film Deposition.....	62
	3.2.1 Selection of Deposition Parameters.....	62
3.3	Structural Characterization of BiMnO ₃ Films on SrTiO ₃ Substrate.....	63
	3.3.1 The Effect of Substrate Deposition Temperature.....	64
	3.3.2 The Effect of Oxygen Pressure.....	67
	3.3.3 The Effect of Post Annealing.....	69
3.4	Determining The Orientation Relationship Between Film and Substrate.....	70

3.5	Magnetic Measurements.....	73
Chapter 4	Conclusions and Future Works.....	76
	References.....	77
	Appendices.....	84
A	Estimation of Errors.....	84
B	Ferroelectric Measurement.....	85
C	User's Manual for Pulsed Laser Deposition (PLD).....	87

List of Figures

Chapter 1

- Figure 1.1 The existence of cross-coupling between ferroelectric, ferromagnetic and ferroelastic properties in a multiferroic material. (Reproduced from [3])..... 16
- Figure 1.2 The magnetic structure of TbMnO_3 . (Reproduced from [16])..... 19
- Figure 1.3 Polarization along the a- and c-axes versus temperature for TbMnO_3 single crystals under different applied magnetic fields. (Reproduced from [7])..... 19
- Figure 1.4 Schematic diagram of the three microstructures for multiferroic composites: (a) particulate composite; (b) multi-layer/superlattice composite; (c) columnar composite. (Reproduced from [19])..... 21
- Figure 1.5 Schematic diagram of a possible multiferroic memory devices based on exchange bias, where white arrows represent the magnetic moments. (Reproduced from [5])..... 22
- Figure 1.6 (a) Schematic diagram of the device used to demonstrate the electrically controllable exchange bias between BiFeO_3 and CoFe . (b) Schematic cross-sectional view of one such device. Magnetic X-ray Circular Dichroism Photoemission Electron microscopy (MXCD-PEEM) images show the ferromagnetic domain structure of the CoFe pillars grown on top of BiFeO_3 in the device. (c) in the as-grown state; (d) after the first electrical switch; (e) after the second electrical switch (Reproduced from [27])..... 24
- Figure 1.7 Schematic diagram of a tunnel junction. Electrons tunnel from

	the bottom electrode through the barrier into the top electrode (Reproduced from [28]).....	25
Figure 1.8	(a) The resistance of LBMO-based spin filters as a function of magnetic field for two different electric fields. Tunnel electroresistance combine with tunnel magnetoresistance, defining four-resistances, label 1-4. (b) Each resistance correspond to different relative orientations of magnetization and polarization. (Reproduced from [29]).....	26
Figure 1.9	Schematic diagram of a magnetostrictive/piezoelectric laminate composite. (Reproduced from [30]).....	27
Figure 1.10	A monoclinic unit cell for the bismuth manganite (BiMnO_3) crystal structure.....	28
Figure 1.11	The electronic configurations for a Mn^{3+} ($3d^4$) ion (Reproduced from [41])	32
Figure 1.12	The magnetic structure of BiMnO_3 . The Bi^{3+} and O^{2-} ions are not shown. The Mn^{3+} ions are purple. (Reproduced from [43]).....	32
Figure 1.13	A portion of the BiMnO_3 crystal structure viewed along the a-axis at 300 K. The black solid lines present the longest Mn-O bond lengths. (Reproduced from [33]).....	33
Figure 1.14	Ferroelectric hysteresis loops for measuring the polarization as a function of the applied electric field for BiMnO_3 samples at different temperatures. (a and b) bulk BiMnO_3 (reproduced from [46] and [47]), (c and d) thin films of BiMnO_3 (Reproduced from [48] and [49]).....	34
Figure 1.15	Variation of dielectric constant with applied magnetic fields at	36

	various temperatures for BiMnO ₃ . (Reproduced from [34]).....	
Figure 1.16	Electrical resistivity versus temperature for BiMnO ₃ . Two anomalies were found at temperatures between 420 and 440 K, and between 750 and 770 K. (Reproduced from [34]).....	37
Figure 1.17	Schematic showing the atomistics of film formation on substrates. (Reproduced from [53]).....	39
Figure 1.18	Schematic diagram showing the epitaxial relationship of TiN (001) grown on Si (001). (a) top view and (b) cross-sectional view. (Reproduced from [54]).....	41
Chapter 2		
Figure 2.1	Schematic diagram of the pulsed laser deposition (PLD) system. (Reproduced from [58]).....	43
Figure 2.2	Schematic illustration of the shape of a plasma plume created by pulsed laser deposition. The angular distribution of the plume is dominated by a cos ⁿ θ function. (Reproduced from [58]).....	44
Figure 2.3	Diffraction of x-rays by planes of atoms.....	47
Figure 2.4	Schematic diagram of PANalytical X'Pert powder diffractometer (front view) (Reproduced from [60]).....	50
Figure 2.5	Schematic diagram of a Philips X'Pert PRO MRD Diffractometer, showing the 2θ, ω, φ and Ψ scan axes. (Reproduced from [61]).....	50
Figure 2.6	Schematic diagram of scanning electron microscopy (Reproduced from [62]).....	52
Figure 2.7	Schematic diagram of PPMS probe showing major components (Reproduced from [65]).....	57

Figure 2.8	Schematic diagram of system components for PPMS VSM option (Reproduced from [65]).....	58
Chapter 3		
Figure 3.1	θ/θ Diffraction pattern for the nominal $\text{Bi}_{1.2}\text{MnO}_3$ target.....	59
Figure 3.2	Scanning electron micrographs of the nominal $\text{Bi}_{1.2}\text{MnO}_3$ target (a) secondary-electron image (b) backscattered electron image....	60
Figure 3.3	diffraction patterns for BiMnO_3 thin films grown with the $\text{Bi}_{1.2}\text{MnO}_3$ target at the temperatures of (a) 700 °C, (b) 650 °C, (c) 640 °C, (d) 630 °C, (e) 625 °C, and (f) 600°C in an oxygen pressure of 75 mTorr. Please see No.1-6 in Table 3.3 for corresponding growth conditions.....	65
Figure 3.4	diffraction patterns for BiMnO_3 thin films grown with the $\text{Bi}_{1.2}\text{MnO}_3$ target at 640 °C in oxygen pressures of (a) 100, (b) 75 and (c) 20 mTorr. Please see No.6-8 in Table 3.3 for corresponding growth conditions.....	68
Figure 3.5	diffraction patterns for (a) the sample subjected to the post annealing process and (b) bare SrTiO_3 substrate. See No.9 in Table 3.2 for corresponding growth conditions.....	70
Figure 3.6	Phi scan of (a) the 110 reflection of the (100)-oriented SrTiO_3 substrate (b) the 400 reflection of the (-202)-oriented BiMnO_3 film deposited on the (100)-oriented SrTiO_3 substrate.....	71
Figure 3.7	Atomic packing of a SrTiO_3 (100) plane.....	71
Figure 3.8	Atomic packing of a BiMnO_3 (-202) plane.....	72
Figure 3.9	Schematic diagram showing the epitaxial relationship of BiMnO_3 (-202) grown on SrTiO_3 (100).....	73

Figure 3.10	ZFC and FC dc-magnetization curves measured as a function of temperature for the BiMnO ₃ thin film in a magnetic field of 100 Oe.....	73
Figure 3.11	Magnetization curves for (a) the prepared BiMnO ₃ film at 20K (b) the BiMnO ₃ film grown by Eerenstein et al (Reproduced from [39]).....	75

List of Tables

Chapter 1

Table 1.1	the coordinates of all of atoms in BiMnO ₃ (From [33]).....	28
Table 1.2	Mn-O bond lengths for MnO ₆ octahedra in BiMnO ₃ (From [33])...	29

Chapter 3

Table 3.1	EDS analysis of the nominal Bi _{1.2} MnO ₃ target.....	61
Table 3.2	A listing of the PLD parameters that were studied. Note: laser fluence (520mJ on a spot size of 0.2cm ²), repetition rate (8Hz), and target-substrate distance (5cm) were fixed for all deposition.....	63
Table 3.3	EDS results for the films grown at 640 °C, 650 °C, and 700 °C.....	67
Table 3.4	Film thicknesses corresponding to substrate deposition temperatures.....	67

Chapter 1 Introduction

1.1 Multiferroic Materials

Magnetic and ferroelectric materials play an important role in every aspect of modern technology. For example, the data storage industry has launched several types memory devices which consist of magnetic or ferroelectric materials [1]. On the other hand, due to the trends toward device miniaturization, the multiferroic materials that combine electric and magnetic properties have received a lot of research interest, so that a single device component is capable of performing more than one function.

The term ‘multiferroic’ was initially mentioned by Schmid to define a material possessing two or more primary ferroic properties (ferroelectricity, ferromagnetism , ferroelasticity) which occur in the same phase [2,3]. Such materials can exhibit cross-coupling between these different properties. Figure 1.1 shows that for a ferroic material, the electric field E , magnetic field H , and stress σ can control the electric polarization P , magnetization M , and strain ϵ , respectively. For a magnetoelectric multiferroic, a magnetic field H may control P , or an electric field E may control M (green arrows).

The coupling between these order parameters can create a new property, termed as the “magnetoelectric coupling”, namely the dependence of magnetic (electric) field on the polarization (magnetization) [4]. The magnetoelectric coupling could yield an entirely novel device, such as electric field–controlled magnetic memory devices that have lower power consumption (for details, see Section 1.2.1.1) [5]. From an applications standpoint, the types of multiferroics that most researchers are interested in are single-phase multiferroics with strong magnetoelectric coupling. Since the discovery

of the first multiferroic materials in 1966, such materials received interest during 1960s and 1970s. However, the research activity has been steadily increasing since several major breakthroughs in 2003-4, including the first observation of large polarization in BiFeO₃ epitaxial thin films in 2003 [6] and the first discovery of strongly coupled multiferroics, TbMnO₃ [7]. Multiferroic materials can be classified into two classes: single phase and composite materials.

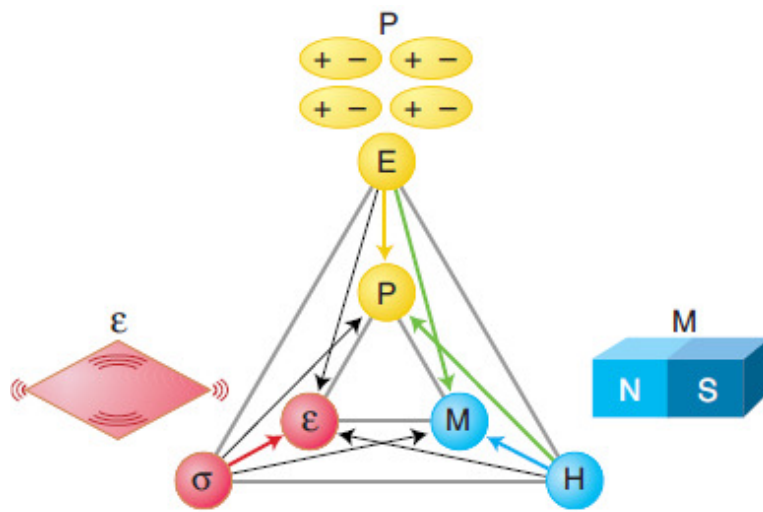


Figure1.1: The existence of cross-coupling between ferroelectric, ferromagnetic and ferroelastic properties in a multiferroic material. (Reproduced from [3])

1.1.1 Single Phase Multiferroic Materials

The first multiferroic material to be discovered in 1966 was Ni₃B₇O₁₃I, which is ferromagnetic and ferroelectric [8]. Some representative multiferroic materials are introduced as follows: For two reasons, the most commonly studied multiferroic material is BiFeO₃. First, BiFeO₃ shows multiferroicity at room temperature and is ferroelectric with a Curie temperature (T_C) around 1103K [9] and antiferromagnetic with a Neil Temperature (T_N) around 643 K [10]. Second, BiFeO₃ epitaxial films show a large ferroelectric polarization (P_r) of 50-60 $\mu\text{C}/\text{cm}^2$ [6] and do not contain

toxic Pb. An important application of ferroelectric materials is Ferroelectric Random Access Memories (FeRAM), and it is desirable that ferroelectric materials used are highly insulating, at room temperature, and have a large switched charge (remanent polarization $>1\mu\text{C}/\text{cm}^2$) [11]. Most multiferroics do not meet these requirements. Usually the operating temperature is too low and the conductivity is too high.

Another commonly studied multiferroic material is BiMnO_3 , which is ferromagnetic with a Curie Temperature (T_C) around 100 K [12]. However, the existence of ferroelectricity in BiMnO_3 remains controversial. The properties and structure of BiMnO_3 are described in Section 1.3 in greater detail. Other examples are the hexagonal manganites which have the general formula RMnO_3 . R is typically a rare earth ion such as Y and Ho. YMnO_3 is antiferromagnetic with a T_N between 70 and 130 K and ferroelectric with a T_C between 570 and 990 K [13]. Many researchers have attributed the rarity of multiferroics to the conflict between magnetism and ferroelectricity (partially filled d orbital vs. empty d orbital) that prevented the simultaneous occurrence of ferromagnetism and ferroelectricity [14].

Multiferroic materials can be classified into two classes [15]. For type I multiferroic materials, ferroelectricity and magnetism have different sources, namely that both of them result from the different subsystems of the material. The origins of ferroelectricity can be due to (i) the existence of a transition metal with d_0 configuration, which has not been found in any multiferroics; (ii) the existence of bismuth or lead where the ferroelectricity is predominantly due to lone pairs of Bi^{3+} and Pb^{2+} , as in BiFeO_3 ; or (iii) the presence of “geometrically driven” ferroelectricity, as in YMnO_3 . However, it was found that the simultaneous presence of polarization and magnetization does not guarantee strong coupling between both of them, because

microscopic mechanisms of ferroelectricity and magnetism are quite different and do not strongly interfere with each other.

For type II multiferroic materials, ferroelectricity is induced by particular magnetically ordered states. For example, TbMnO_3 has two different magnetic ground states which occur below $T_{N1}=41\text{K}$ and $T_{N2}=28\text{K}$, respectively. Ferroelectricity only exists in the lower temperature magnetic ground state, which has a spiral magnetic structure with rotating magnetic moments, as shown in figure 1.2 [16]. The wave vector (Q) is parallel to the b-axis, and spins rotate around the a-axis, inducing polarization parallel to the c-axis. A plausible microscopic mechanism inducing ferroelectricity in magnetic spirals is discussed in ref 17.

Figure 1.3 shows the temperature dependence of polarization along c- and a- axes at different magnetic fields. While increasing magnetic fields from 0T to 9T, the spontaneous polarization is found to be switched from the direction along the c-axis to the direction along the a-axis, and hence rotated by 90° . Obviously, type II multiferroic materials can exhibit a stronger magnetoelectric coupling, namely that magnetic field can greatly influence the polarization. Therefore, type II multiferroic materials are of considerable interest and have attracted a number of theoretical and experimental investigations.

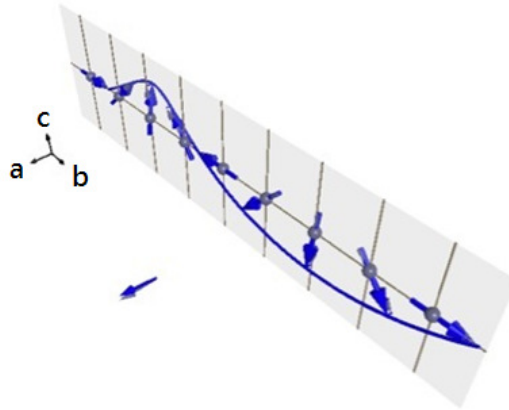


Figure 1.2 The magnetic structure of TbMnO_3 . (Reproduced From [16])

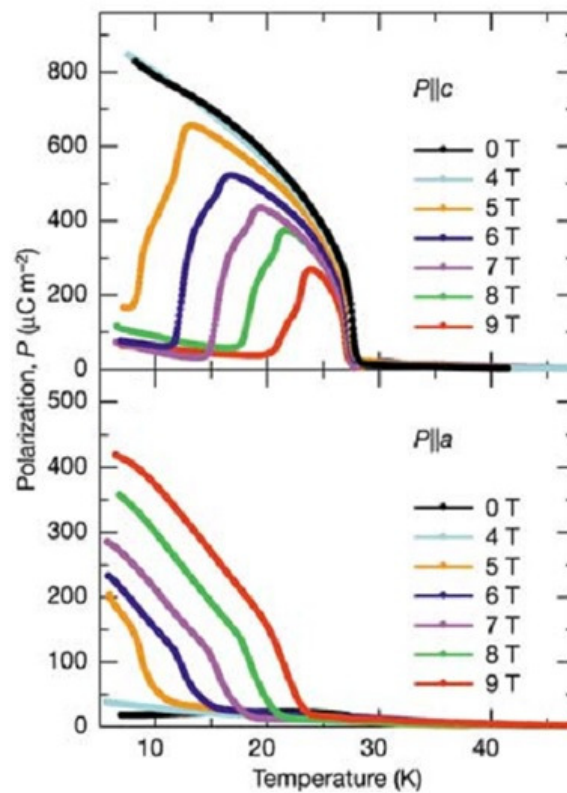


Figure 1.3 Polarization along the a- and c-axes versus temperature for TbMnO_3 single crystals under different applied magnetic fields. (Reproduced from [7])

1.1.2 Composite Multiferroic Materials

The practical applications of single phase multiferroic materials are limited for several

reasons. First, in most single phase multiferroic materials, these order parameters only co-exist at low temperature. Second, the polarization and magnetization is typically small for type I and II. Third, the magnetoelectric coupling for type I multiferroics is weak [18].

Artificial composites of piezoelectric (ferroelectric) and ferromagnetic phases have been proposed and received a lot of interest [19]. Note that ferroelectric materials must have piezoelectricity, while the piezoelectric materials do not necessarily have ferroelectricity [20]. The magnetoelectric effect is due to the fact that the mechanical deformation due to magnetostriction results in a dielectric polarization due to the piezoelectric effect [19]. To maximize the magnetoelectric coupling, components with larger magnetostrictive coefficients and large piezoelectric coefficients are preferred.

The magnetoelectric coupling in bulk composites is typically weak due to the presence of microcracks, defects, impurities and leakage currents in the sintered composites, so the layered and nanostructured composites have been proposed [18]. Multiferroic composite thin films could have three different types of microstructures (Figure 1.4) as demonstrated in bulk composites, namely particulate structure, multilayer/ superlattice structure, and columnar structure. Examples include i) multilayer heterostructures with alternating layers of nickel ferrite (NFO) and lead zirconate titanate (PZT) [21], ii) multilayer heterostructures with alternating layers of lanthanum strontium manganites (LSMO) and lead zirconium titanate (PZT) [22], and iii) BaTiO_3 - CoFe_2O_4 films with spinel CoFe_2O_4 nanopillars embedded in the perovskite BaTiO_3 matrix [23]. All of them were found to have significant magnetoelectric coupling.

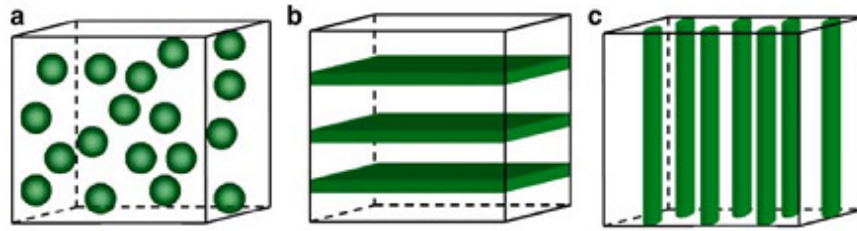


Figure 1.4 Schematic diagram of the three microstructures for multiferroic composites: (a) particulate composite; (b) multi-layer/superlattice composite; (c) columnar composite. (Reproduced from [19])

1.2 Possible Applications of Multiferroic Materials

Multiferroic materials can play an important role in the electronic industry when developing a large magnetoelectric coupling. Potential technological applications have been suggested including magnetic field sensors, memory devices, and transducers [11]. A brief presentation of magnetic field sensors and memory devices which seem relevant to this research are described below.

1.2.1 Memory Devices

Today computer information is encoded as patterns of 0s and 1s [24]. These digits are called bits. The patterns of bits can be used to represent numeric values, characters in an alphabet, images or sounds. In order to create bit 0 and bit 1, at the heart of every memory is some measurable attribute that can assume at least two relatively stable states [25]. So far two types of memory devices based on multiferroic materials have been presented.

1.2.1.1 Memory Devices Based on Exchange Bias

The first type of memory devices are based on exchange bias [5], which occurs at the

interface between ferromagnetic and antiferromagnetic materials, and the magnetic moments in the ferromagnetic layer will be coupled to the magnetic moments in the antiferromagnetic material. The structure of this type of memory device is shown in Figure 1.5, where there is a trilayer on top of a multiferroic material (green), which is ferroelectric and antiferromagnetic. Two ferromagnetic layers (blue) are separated by an insulating tunneling barrier (red). The relative orientations of both of the ferromagnetic layers determine the resistance of the structure. Parallel alignment allows current flow, and antiparallel alignment blocks current flow.

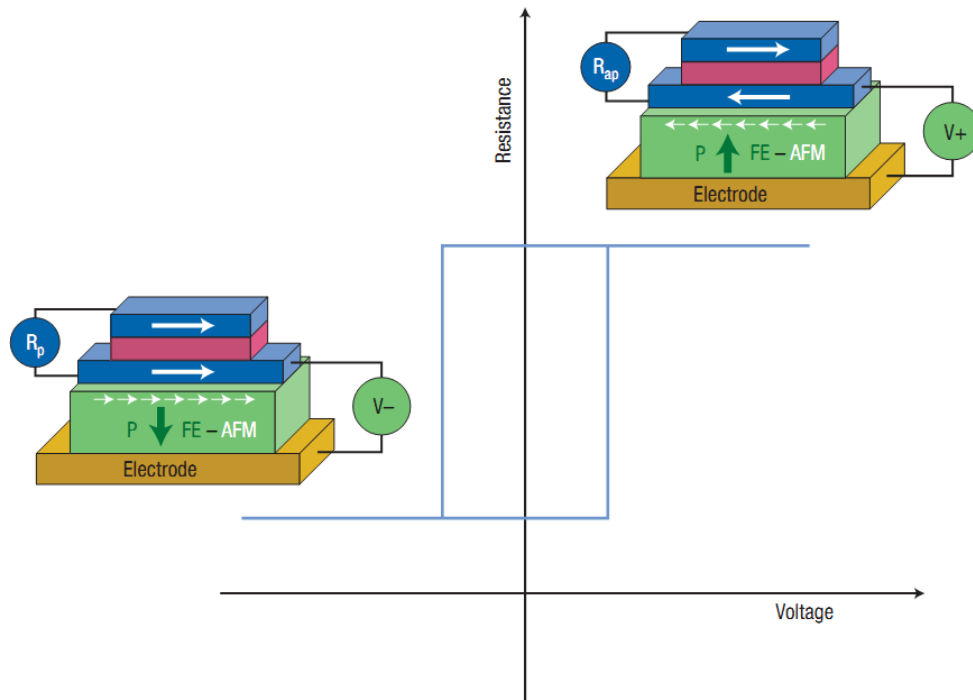


Figure 1.5 Schematic diagram of a possible multiferroic memory devices based on exchange bias, where white arrows represent the magnetic moments. (Reproduced from [5])

If the magnetoelectric coupling of the multiferroic material is strong enough, the magnetization in the multiferroic can be reversed by applying an electric field across the multiferroic, further changing the magnetization of the ferromagnetic layer on top of it via exchange bias. The relative orientations of both of the ferromagnetic layers determine the resistance of the structure. Parallel alignment allows current flow, and antiparallel alignment blocks current flow.

whereas antiparallel has a high resistance. Therefore the parallel and antiparallel arrangements can represent bit 1 and bit 0.

Such a multiferroic memory device has a significant advantage over magnetoresistive random-access memory (MRAM), i.e. it has lower power consumption. For MRAM, the writing process involves the switching of magnetization with magnetic field, and the required energy barrier is at least $50\text{-}60k_{\text{B}}T$, where k_{B} is the Boltzmann constant and T is temperature [26]. Therefore, a large writing current that can give rise to the field is needed in MRAM to switch the magnetization into the opposite direction.

Chu et al. have experimentally demonstrated this concept using a specially designed device [27], as shown in Figure 1.6 (a) and (b). It was found that the ferromagnetic domain structure of CoFe micrometre-size elements deposited on top of a BiFeO₃ film also exhibits a systematic coupling with the antiferromagnetic spins in BiFeO₃. When an in-plane electric field is applied, the magnetic domain structure of the CoFe dots is modified because the magnetization rotates by 90 degrees, as shown in Figure 1.6 (c)-(d). The original magnetic state is recovered when a voltage with opposite polarity is applied.

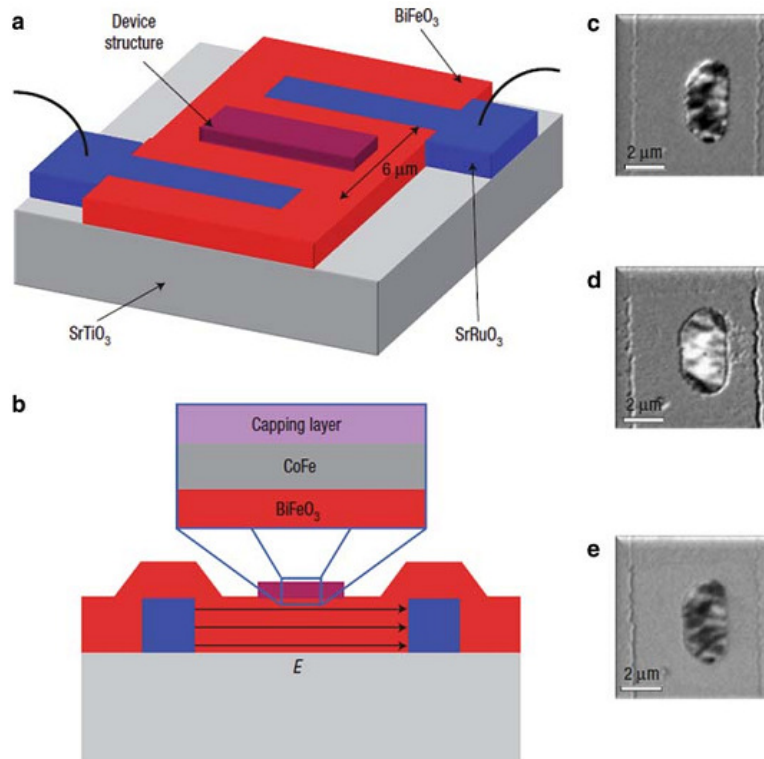


Figure 1.6 (a) Schematic diagram of the device used to demonstrate the electrically controllable exchange bias between BiFeO₃ and CoFe. (b) Schematic cross-sectional view of one such device. Magnetic X-ray Circular Dichroism Photoemission Electron microscopy (MXCD-PEEM) images show the ferromagnetic domain structure of the CoFe pillars grown on top of BiFeO₃ in the device. (c) in the as-grown state; (d) after the first electrical switch; (e) after the second electrical switch (Reproduced from [27])

1.2.1.2 Memory Devices Based On Tunneling Magnetoresistance

The second type of memory devices are based on tunneling magnetoresistance, as shown in Figure 1.7 [28]. The structure of this memory device is a multiferroic tunnel junction. Gajek et al. first produced this device by using 2 nm-thick La_{0.1}Bi_{0.9}MnO₃ (LBMO) thin films, which remain ferromagnetic and ferroelectric, as a barrier, 30 nm-thick La_{2/3}Sr_{1/3}MnO₃ (LSMO) thin films as a bottom electrode, and Au as a top electrode [29].

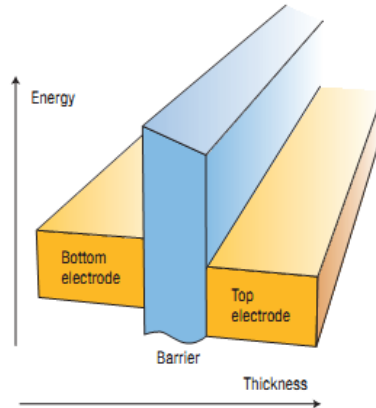


Figure 1.7 Schematic diagram of a tunnel junction. Electrons tunnel from the bottom electrode through the barrier into the top electrode (Reproduced from [28])

Such a device was found to show Tunnel Magnetoresistance Effect (TMR) and Electroresistance Effect (ER). TMR effect is defined as $TMR = (R_{ap} - R_p) / R_p$, that is, the difference between the junction resistances with the antiparallel and parallel configurations of the LSMO and LBMO magnetizations. Electroresistance (ER) is the change in resistance of a material under an applied electric field. ER is defined by $ER = [R(E) - R(0)] / R(0)$, where $R(E)$ and $R(0)$ are the resistances under the electric fields of E and 0. It is possible to combine both ER and TMR to obtain four different resistance states at low bias voltage, as labeled 1-4 in Figure 1.8 (a), further creating four bits. Four bits can allow an exponentially increased computing capacity. Thus, this type of memory device is a significant breakthrough in the quest for the ultimate memory device.

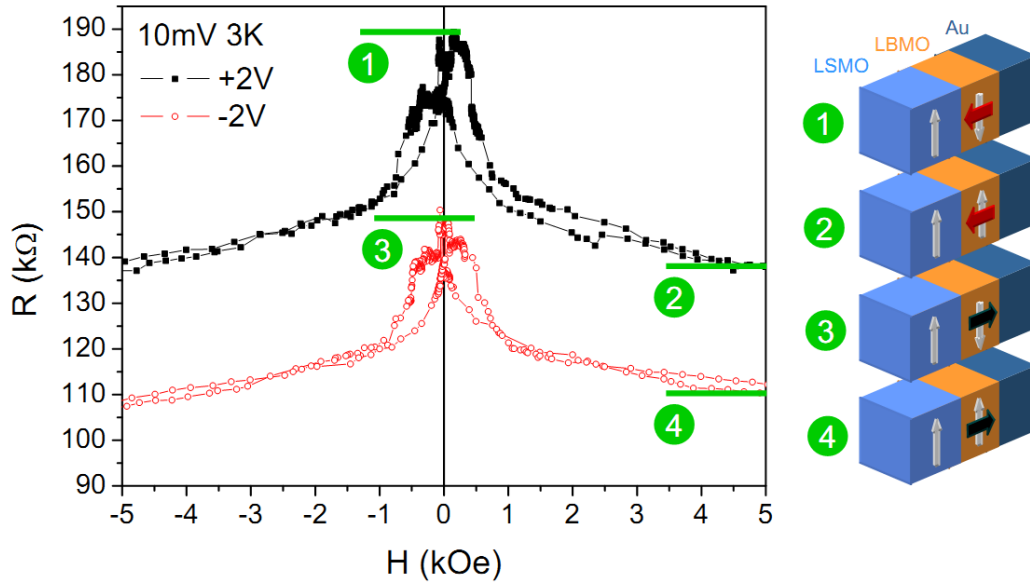


Figure 1.8 (a) The resistance of LBMO-based spin filters as a function of magnetic field for two different electric fields. Tunnel electroresistance combines with tunnel magnetoresistance, defining four-resistances, label 1-4. (b) Each resistance corresponds to different relative orientations of magnetization (white) and polarization (red and black). (Reproduced from [29])

1.2.2 Magnetic Field Sensors

Composites which consist of a magnetostrictive material and a piezoelectric material can be used to probe a small magnetic field. The principle is that when experiencing a magnetic field, the magnetostrictive material makes a strain and hence a stress, and then the piezoelectric material subjected to the stress generates a polarization and hence a voltage. The most commonly used magnetostrictive material is Terfenol-D, while the most commonly used piezoelectric material is PZT. Various device structures have been developed. One representative structure, as shown in Figure 1.9, is a laminate which consists of two Terfenol-D ($Tb_{1-x}Dy_xFe_{2-y}$) layers magnetized in their length directions, and two hard PZT piezoelectric ceramic layers also poled

longitudinally [30]. Such a structure was found to show dramatically enhanced magnetoelectric effects.

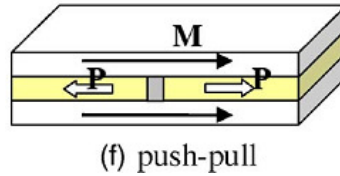


Figure 1.9 Schematic diagram of a magnetostrictive/piezoelectric laminate composite. (Reproduced from [30])

1.3 Bismuth Manganite (BiMnO_3)

The crystal structure of BiMnO_3 has been examined several times. In 1965, Sugawara et al. reported that BiMnO_3 was a triclinically distorted pseudo-cubic perovskite with $a = c = 3.935 \text{ \AA}$, $b = 3.989 \text{ \AA}$, $\alpha = \gamma = 91.43^\circ$, $\beta = 91.03^\circ$ [31]. In 1999, Atou et al. determined that BiMnO_3 has a monoclinic unit cell ($a = 9.5323 \text{ \AA}$, $b = 5.6064 \text{ \AA}$, $c = 9.8535 \text{ \AA}$, and $\beta = 110.667^\circ$) with non-centrosymmetric $C2$ space group [32]. In 2007, Belik et al. reported that the crystal structure of BiMnO_3 belongs to centrosymmetric space group $C2/c$, and has a monoclinic unit cell with lattice parameters $a = 9.5415 \text{ \AA}$, $b = 5.61263 \text{ \AA}$, $c = 9.8632 \text{ \AA}$, $\beta = 110.6584^\circ$ [33] (See figure 1.10). The result by Belik et al. is extensively accepted in recent papers, such monoclinic indices are thus used throughout this thesis to describe the crystal structure of these BiMnO_3 films.

The coordinates of all the atoms are listed in Table 1.1, and the number of BiMnO_3 units in the unit cell is equal to eight [33]. There are two different Mn atoms specified, labeled Mn1 and Mn2. Each of these atoms will be replicated four times, by the action of the symmetry axis, so that the unit cell will contain eight atoms of manganese. Similarly, there are three different O atoms listed, labeled O1, O2 and O3, giving

twenty-four atoms of oxygen in the unit cell.

Table 1.1 the coordinates of all of atoms in BiMnO₃ (From [33])

site	Wyckoff position	x	y	z
Bi	8f	0.136 38	0.218 32	0.126 17
Mn1	4e	0	0.2115	0.75
Mn2	4d	0.25	0.25	0.5
O1	8f	0.099 80	0.1723	0.581 45
O2	8f	0.145 78	0.5714	0.367 95
O3	8f	0.354 34	0.5484	0.164 71

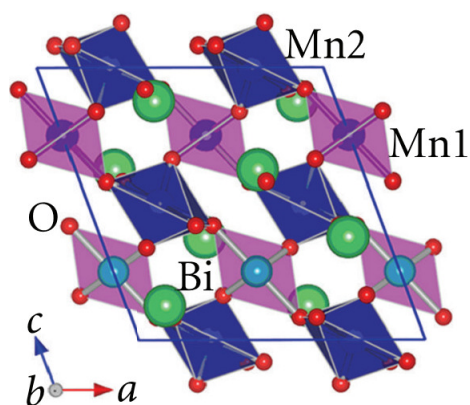


Figure 1.10 A monoclinic unit cell for the bismuth manganite (BiMnO₃) crystal structure.

It was found that the MnO₆ octahedra in BiMnO₃ are strongly distorted. At 300K, two MnO₆ octahedra are elongated along one axis in BiMnO₃, and both of them have two long distances (~2.2Å) and four short distances (~1.95Å), as shown in Table 1.2. It can be attributed to the Jahn-Teller distortion of Mn³⁺ ions with d⁴ configuration. This spontaneous distortion has been theoretically proved to be energetically favourable.

Table 1.2 Mn-O bond lengths for MnO₆ octahedra in BiMnO₃ (From [33])

	Bond Lengths (Å)		Bond Lengths (Å)
Mn1-O1 (×2)	2.199	Mn2-O1 (×2)	1.924
Mn1-O2 (×2)	1.906	Mn2-O2 (×2)	2.242
Mn1-O3 (×2)	1.986	Mn2-O3 (×2)	1.941

At ambient pressure, BiMnO₃ can go through two structural transitions [34, 35, 36]. The structural transition at T = 474K is the change in the structure from monoclinic C2/c(I) to monoclinic C2/c(II). The structural transition from monoclinic C2/c(II) to orthorhombic Pnma occurs at T=760K. BiMnO₃ decomposes above the temperature of 770K in air.

BiMnO₃ is not stable at atmospheric pressure, and it requires pressures of approximately 6 GPa and temperatures of approximately 1100 K to be fabricated in bulk from a mixture of Bi₂O₃ and Mn₂O₃ [33]. Under ambient pressure the reaction of the metal oxides is $\text{Bi}_2\text{O}_3 + \text{Mn}_2\text{O}_3 \rightarrow \frac{1}{2}\text{Bi}_2\text{Mn}_4\text{O}_9 + \frac{1}{2}\text{Bi}_2\text{O}_3$ [37] and it is therefore an inaccessible material for research via this synthesis route.

However, thin film deposition processes provide another approach to fabricate BiMnO₃. Some research groups have successfully grown epitaxial BiMnO₃ using epitaxial stabilization, namely the use of interfacial strain energy to grow the desired metastable phase rather than the equilibrium phase. Thin film BiMnO₃ has been grown in epitaxial form on SrTiO₃ [38, 39, 40].

1.3.1 Ferromagnetism of BiMnO₃

The fundamental object in magnetism is the magnetic moment, which can be thought of as resulting from an infinitesimal current loop in classical electromagnetism [41]. In an atom, the magnetic moment has two sources. The first one is associated with the electron's orbital motion around the nucleus, while the second one is the electron intrinsic angular momentum (spin). Thus when it comes to magnetism, one has to consider the electronic configuration of an atom, i.e. how the orbitals are filled with electrons. It is known that only atoms with a partially filled shell can produce magnetic moment, while the atom with a filled shell has electron spins cancelled out with each other, leaving no magnetic moment. BiMnO₃ contains Mn³⁺ ions with electronic configuration of [Ar] 3d⁴. The d orbitals fall into two classes, the t_{2g} orbitals which point between the x, y and z axes (these are the d_{xy}, d_{xz} and d_{yz} orbitals) and the e_g orbitals which point along these axes (the d_{z²} orbital, which has lobes which point along the z axis and the d_{x²-y²} orbital, which has lobes which point along both the x-and y-axes) [41].

In the case of a gaseous Mn³⁺ ion, i.e. a single, isolated ion with all other atoms located an infinite distance away, the five 3d orbitals have the same energy. The four electrons reside singly in different d orbitals, according to Hund's rule, and the Mn³⁺ ion has all of the four unpaired electrons in d orbitals have parallel spins.

When the Mn³⁺ ion is part of an octahedron MnO₆, the five d orbitals do not have identical energies. In an octahedral environment, for example, the d orbitals divide into two groups: a higher-energy group (d_{z²} and d_{x²-y²}) and a lower-energy group (d_{xy}, d_{xz} and d_{yz}) due to the overlap between neighbouring orbitals. Moreover, since BiMnO₃ have highly distorted octahedra with a stretch along the z- axis and a

contract ion along the x- and y- axes, so $d_{x^2-y^2}$ has a higher energy than d_{z^2} , and d_{xy} has a higher energy than d_{xz} and d_{yz} [41]. Electrons tend to fill the d orbitals in a manner that leads to the lowest total energy. For the electron configurations of d^4 , two electron configurations can occur, namely high spin configuration (with the maximum number of unpaired electrons, in this case 4) and low spin configuration (containing the minimum number of unpaired electrons, in this case 2). The precise order in which the orbitals are filled depends on the competition between the crystal field energy and the Coulomb energy cost of putting two electrons in the same orbital, which is known as the pairing energy [41].

Magnetic measurements can determine whether a compound is high spin or low spin, since there is a theoretical relation between the magnetic moment and the number of unpaired electrons, namely

$$\mu_{\text{eff}} = 2\mu_B\sqrt{S(S+1)}$$

where μ_{eff} is the theoretical value of magnetic moment, μ_B is Bohr magneton, and S is spin angular momentum associated with the number of unpaired electrons [41]. For the case of the 3d ions, the orbital angular momentum (L) is said to be quenched and thus can be effectively ignored. This effect is known as orbital quenching [41].

BiMnO_3 was found to have a magnetic moment of $3.77\mu_B$ on each Mn^{3+} ion [43]. If the number of unpaired electrons is 4 (it would be the case of high spin configuration), and $S = 4 \times \frac{1}{2} = 2$, the theoretical value of magnetic moment is expected to be $4.90\mu_B$. If the number of unpaired electrons is 2 (it would be the case of low spin configuration), and $S = 2 \times \frac{1}{2} = 1$, the theoretical value of magnetic moment is expected to be $2.83\mu_B$.

Because the measured value should be less than the theoretical value, the Mn^{3+} ion in

BiMnO₃ is said to have a high-spin configuration [44], as shown in Figure 1.11.

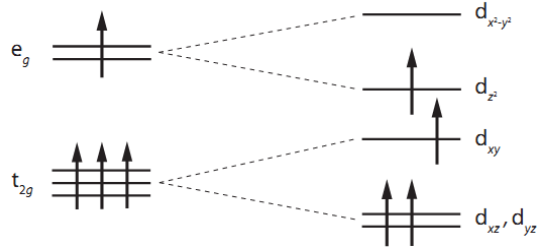


Figure 1.11 The electronic configurations for a Mn³⁺ (3d⁴) ion (Reproduced from [41])

Bulk BiMnO₃ shows one ferromagnetic transition at T_C = 101 K [42,43]. From the result of the magnetic structure refinements at 20 K, BiMnO₃ was found to have a collinear magnetic structure with the magnetic moment of 3.77μ_B aligned along the monoclinic b-axis [43], as shown in Figure 1.12, which is close to the expected value of 4.9μ_B. Magnetic properties of thin-film samples differ from those of bulk BiMnO₃. Thin films usually have the reduced T_C: 97K [38], 85K [39]. All thin-film samples have strongly reduced saturated magnetization [38, 39].

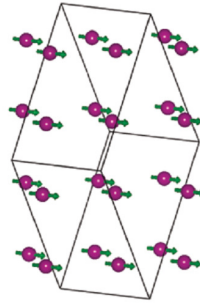


Figure 1.12 The magnetic structure of BiMnO₃. The Bi³⁺ and O²⁻ ions are not shown. The Mn³⁺ ions are purple. (Reproduced from [43])

The ferromagnetic structure of BiMnO₃ in which all the magnetic moments are in parallel alignment was attributed to the peculiar orbital ordering of the C2/c(I) phase [44,45]. It can be explained by considering the superexchange interactions, namely

that an indirect exchange interaction between non-neighbouring magnetic ions is mediated by a non-magnetic ion placed in between the magnetic ions. Figure 1.13 shows that the MnO_6 octahedral environment (green) is found in the crystal structure of BiMnO_3 where oxygen anions O^{2-} sit on the corners of an octahedron with the metal atom Mn at the centre. The magnetic Mn ion in each octahedron interacts with the magnetic Mn ions in six neighboring octahedra via the mediation of non-magnetic O^{2-} ions. According to the rules proposed by Goodenough and Kanamori, in four of the six Mn-O-Mn pathways, the half filled d_{z^2} orbitals point towards the empty $d_{x^2-y^2}$ orbitals on the next manganese; such interactions are predicted to be ferromagnetic. In two of the six Mn-O-Mn pathways, the empty $d_{x^2-y^2}$ orbitals point towards each other; such interactions are predicted to be weak antiferromagnetic. There should be four ferromagnetic (FM) interactions and two antiferromagnetic (AFM) interactions. It is believed that the ferromagnetic interactions overcome the antiferromagnetic interactions below the critical temperature, and consequently, the ferromagnetism of BiMnO_3 appears.

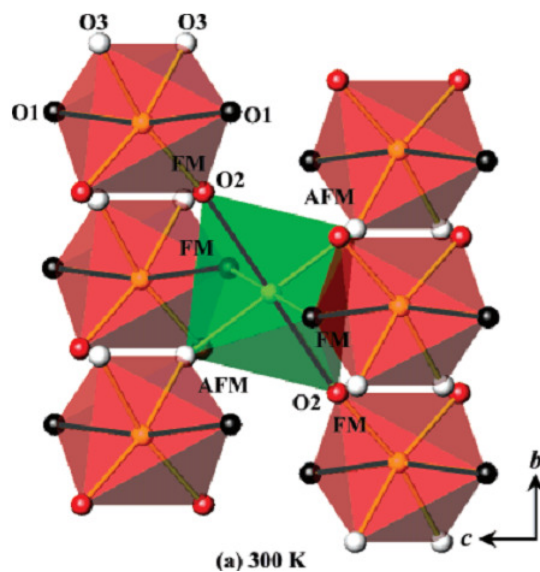


Figure 1.13 A portion of the BiMnO_3 crystal structure viewed along the a-axis at 300 K. The black solid lines show the longest Mn-O bond lengths. (From [33])

1.3.2 Ferroelectricity of BiMnO₃

The existence of ferroelectricity in BiMnO₃ remains controversial. For the bulk samples, some BiMnO₃ bulks were found to show ferroelectricity, with weak remanent polarization values of 0.043 $\mu\text{C}/\text{cm}^2$ at 200 K [46] and 0.06 $\mu\text{C}/\text{cm}^2$ at room temperature [47] (See Figure 1.14(a) and (b)). No ferroelectricity is found in some BiMnO₃ bulks, and such results are rarely mentioned [36]. For the thin film samples, some BiMnO₃ thin films were found to show ferroelectricity, with weak remanent polarization values of 9 and 16 $\mu\text{C}/\text{cm}^2$ at room temperature [48] and 23 $\mu\text{C}/\text{cm}^2$ at 5K [49] (See Figure 1.14(c) and (d)). No ferroelectricity is found in some BiMnO₃ thin films, and such results are rarely mentioned [36]. (A description of ferroelectric measurement may be found in Appendix B.)

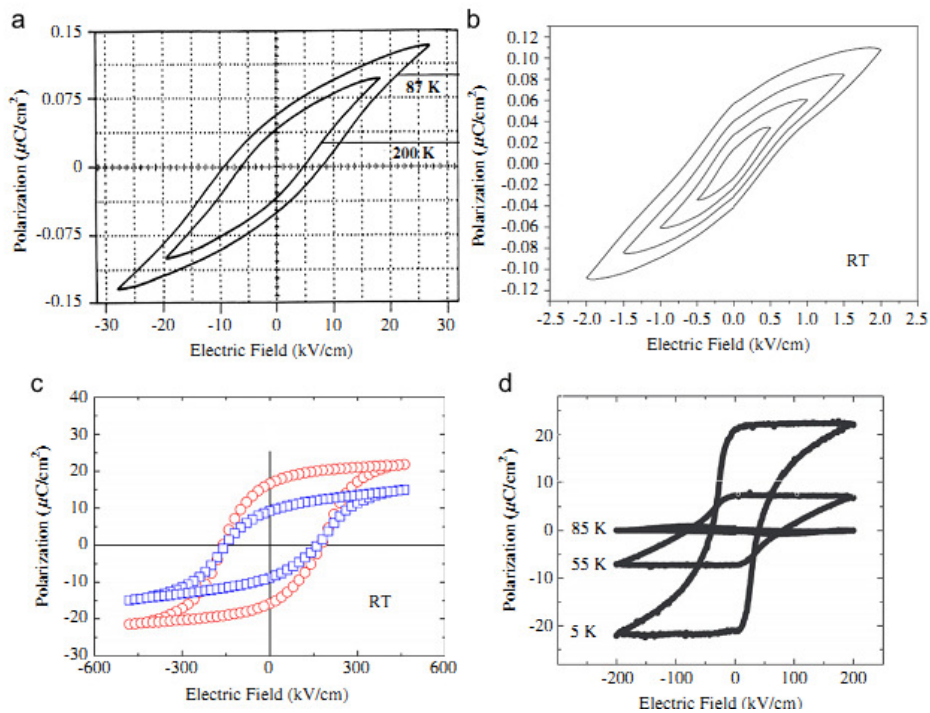


Figure 1.14 Ferroelectric hysteresis loops for measuring the polarization as a function of the applied electric field for BiMnO₃ samples at different temperatures. (a and b) bulk BiMnO₃ (reproduced from [46] and [47]), (c and d) thin films of BiMnO₃ (reproduced from [48] and [49]).

Some theoretical research [50] claimed that BiMnO₃ belongs to centrosymmetric C2/c space group with zero ferroelectric polarization. Although the Bi³⁺ lone pairs lead to strong local polar distortions, the relative orientations of adjacent lone pairs are opposite to each other and equivalent, leading to an antiferroelectric arrangement. Additional studies [51] claimed that BiMnO₃ crystallized in the centrosymmetric C2/c structure, but the centrosymmetric C2/c symmetry in BiMnO₃ is spontaneously broken by hidden antiferromagnetic interactions, further inducing the ferroelectricity.

1.3.3 Magnetolectric Coupling of BiMnO₃

A correct description of magnetolectric coupling needs to measure the effect of a magnetic field on ferroelectric polarization or, conversely, that of an electric field on magnetic order. A difficulty in achieving this is that many candidates considered to be magnetolectric are in fact poor insulators, which make them difficult to sustain the electric fields required to switch polarization [52]. Moreover, for a multiferroic material, magnetization may be coupled to polarization that is associated with the dielectric constant as well. Therefore, the magnetolectric coupling can also be measured indirectly by recording the dielectric constant as a function of temperature and magnetic field [52].

Kimura et al. reported [34] the dielectric constant (ϵ) of BiMnO₃ varies with the magnetic field, as shown in Figure 1.15. The phenomenon is called magnetocapacitance effect, which is defined as

$$\frac{\Delta\epsilon(H)}{\epsilon(0)} = \frac{\epsilon(H) - \epsilon(0)}{\epsilon(0)}$$

where $\epsilon(H)$ and $\epsilon(0)$ are the dielectric constant at certain field and zero field, respectively. For temperatures far below a magnetic transition temperature around

100K, the value of magnetocapacitance is negligibly small. As the temperature is raised, the value of magnetocapacitance increases, showing a maximum near 100K. When further raising to the temperature above 100K, the magnetocapacitance decreases again.

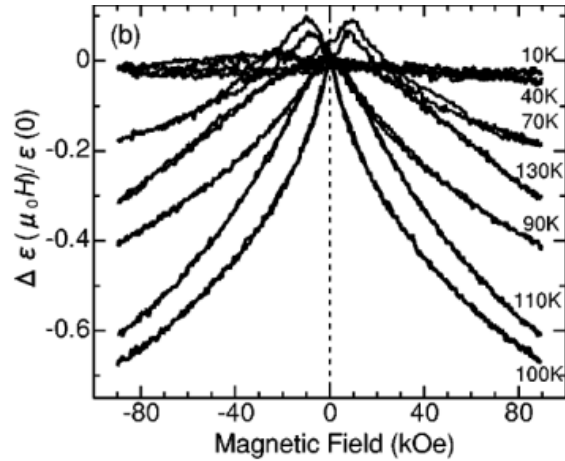


Figure 1.15 Variation of dielectric constant with applied magnetic fields at various temperatures for BiMnO₃. (Reproduced from [34])

1.3.4 Electronic Properties of BiMnO₃

The temperature dependence of the resistivity of BiMnO₃ was recorded as the temperature was cycled between 300K and 800K, as shown in Figure 1.16. The resistivity of BiMnO₃ decreases with increasing temperature. An important point to notice is that the resistivity curve for BiMnO₃ shows two anomalies at the temperatures around 474K and 760K, corresponding to two structural transitions.

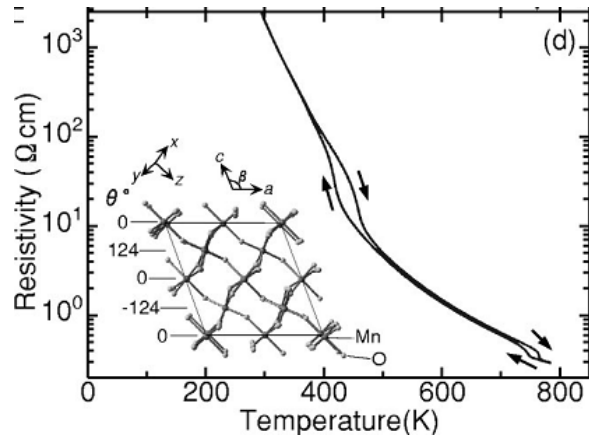


Figure 1.16 Electrical resistivity versus temperature for BiMnO₃. Two anomalies were found at temperatures between 420 and 440 K, and between 750 and 770 K. (Reproduced from [34])

1.4 Modes of Film Growth by Vapor Deposition

Pulsed laser deposition (PLD) is a vapor deposition technique, which refers to any process in which a solid immersed in a vapor becomes larger in mass due to transfer of material from the vapor into the solid surface [53]. Vapor deposition film formation has two stages: first, from vapor to adatoms and second, from adatoms to film growth.

At the first stage, a clean surface of the substrate material at temperature T_s is exposed to a vapor of a chemically compatible film material at the temperature T_v . Atoms in the vapor come into contact with the substrate surface where they form chemical bonds with atoms in the substrate. Therefore, adatoms become attached to the substrate. There is a reduction in energy due to formation of the bonds during attachment. At the second stage, due to thermal activation, surface diffusion results, the adatoms are able to migrate over the surface [53].

Modes of film growth can be classified into three classes, as shown in Figure 1.17.

The first type is that film growth tends to perform in a layer by layer mode. Adatoms are more likely to attach to the substrate surface than to other film material surfaces. Once small stable clusters of adatoms form on the surface, other adatoms tend to attach to the cluster at its periphery where they can bond with both substrate and film atoms, thereby continuing the planar growth. This layer-by-layer film growth mode is often called the Frank—van der Merwe growth mode (or FM mode). The second type is that adatoms form three-dimensional clusters or islands on the surface of the substrate. Film growth proceeds by the growth of islands until they coalesce; this type of growth is commonly called the Volmer—Weber growth mode (or VW mode). A third type of growth is called the Stranski—Krastanov growth mode (or SK mode), where after a few monolayers of film material are formed, subsequent adatoms prefer to gather into clusters over continue planar growth.

Thin film deposition can be performed by many deposition methods. There may be an enormous variation in the microstructures of films of the same material. Final structures can range from single crystal films, through polycrystalline films, to largely amorphous films. The final microstructure depends on the materials involved, the deposition method used and the environmental constraints imposed. The term “epitaxy” means that the thin films are grown in a particular crystallographic orientation with respect to the substrate. Such thin films are characterized by single crystals with low defect density. When the film material is the same as the substrate material, crystallographic registry between the film and the substrate is commonly referred to as homoepitaxy. The epitaxial deposition of a film material that is different from the substrate material is known as heteroepitaxy [53].

The other advantage of epitaxy is that metastable crystallographic phases can be

grown by appropriately choosing a substrate on which to grow the film. Thin film growth on crystalline substrates allows the forces present at the interface to drive the film into a different crystallographic phase. This metastable phase may already be known as a high temperature or high pressure phase. The phenomenon is often referred to as “epitaxial stabilization” [54]. The epitaxial growth of extremely high quality single-layer complex oxide materials can be achieved by using atomically flat substrates and specific film-deposition methods. In heteroepitaxial film growth, the substrate crystal structure provides a template for positioning the first arriving atoms of film material, and each atomic layer of film material serves the same function for the next layer to be formed by FM growth.

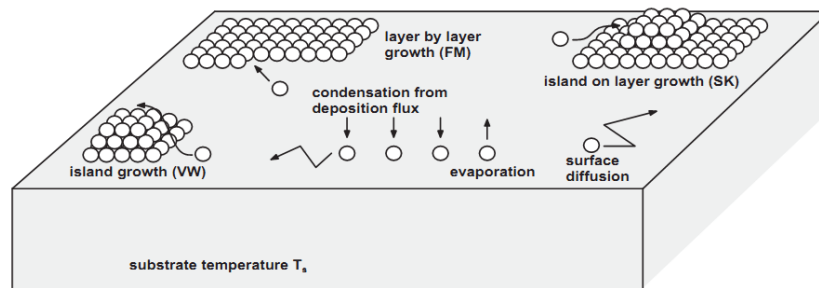


Figure 1.17 Schematic showing the atomistics of film formation on substrates. (Reproduced from [53])

1.4.1 Domain Matching Epitaxy (DME)

In the conventional theory of epitaxial growth, called lattice matching epitaxy (LME), thin films are epitaxially grown with one-to-one matching of lattice constants across the film–substrate interface as long as the lattice misfit between the film and the substrate is less than 7%– 8%. Lattice misfit (f) is defined by

$$f = \frac{a_s - a_f}{a_f}$$

where a_f and a_s are lattice constants of the film and the substrate, respectively. Above a lattice misfit of 7%– 8%, it was surmised that the film will grow largely

polycrystalline. However, lattice matching epitaxy (LME) theory has been proved to be incorrect, with several groups reporting the successful epitaxial growth of TiN films on Si substrate with a lattice misfit of 28% for cube-on-cube TiN ($a=0.424$ nm) epitaxy over silicon ($a=0.543$ nm) [55]. Thus, the concept of domain matching epitaxy (DME) has been proposed and generalized. Domain matching epitaxy (DME) involves the matching of certain lattice planes of the film and substrate, both of which have similar crystal symmetry. In DME, initial misfit strain is defined by

$$f = \frac{d_s - d_f}{d_f}$$

where d_f and d_s are the certain inter-planar spacing of the film and the substrate. The initial misfit strain can be relaxed by matching of m planes of the film with n of the substrate, leaving a residual strain of

$$\varepsilon_r = (md_f/nd_s - 1)$$

In the case of a perfect matching $md_f = nd_s$, and the residual strain ε_r is zero. If the domain matching is not perfect, epitaxy occurs by accommodating the additional misfit by changing the domain size [55].

For instance, TiN thin films were found to be epitaxially grown on Si substrate with the out-of-plane orientation relationship of $\text{TiN}(001) \parallel \text{Si}(001)$ [56]. Four unit cells of TiN match three unit cells of Si very well. One can obtain that $d_{\text{TiN}} = 0.424$ nm, $d_{\text{Si}} = 0.543$ nm, $m=4$, and $n=3$. Although the system has a large initial misfit strain of 28% ($f = (d_{\text{Si}} - d_{\text{TiN}}) / d_{\text{TiN}}$), the initial misfit strain can be relaxed by matching of m planes of the film with n of the substrate, leaving a residual strain of 4% ($\varepsilon_r = (md_{\text{TiN}}/nd_{\text{Si}} - 1)$). Schematic diagram of TiN/Si epitaxial system is shown in Figure 1.18.

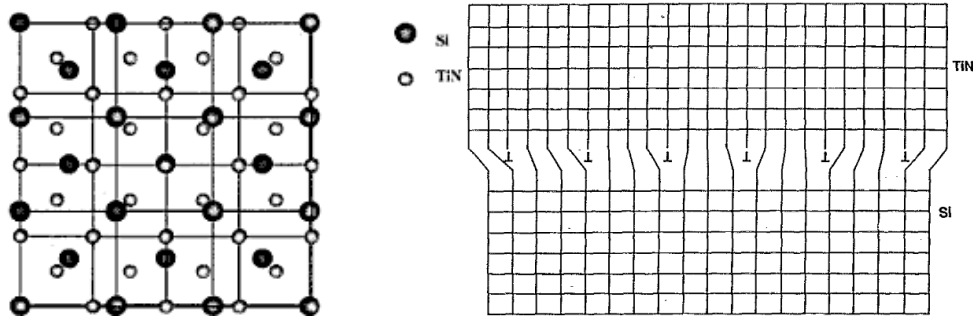


Figure 1.18 Schematic diagram showing the epitaxial relationship of TiN (001) grown on Si (001). (a) top view and (b) cross-sectional view. (Reproduced from [56])

1.5 Research Problems

Unlike most single phase multiferroics (such as BiFeO_3 and YMnO_3) that show antiferromagnetic and ferroelectric ordering, BiMnO_3 has been found to be ferromagnetic and possibly ferroelectric so that it can provide more degrees of freedom in the possible applications. In addition, Gajek et al. [29] demonstrated that when BiMnO_3 was doped with La, the magnetoelectric effect was facilitated, and both ferromagnetic and ferroelectric properties were retained down to a film thickness of 2 nm. Hence, single phase BiMnO_3 is a promising material worth being explored and developed. This is the purpose of my thesis and thus will now be described in detail.

Chapter 2 Experimental Techniques

In this research, epitaxial BiMnO_3 thin films were deposited on SrTiO_3 substrates using pulsed laser deposition (PLD). The structural and magnetic characterizations of these films were performed. The research could be divided into three parts. First, a PLD target was prepared and characterized. Second, the growth of the thin films was carried out. Third, structural and magnetic characterizations of these films were performed. The experimental techniques involved in this research will be introduced in the following sections.

2.1 Pulsed Laser Deposition (PLD) of Thin Films

Pulsed laser deposition (PLD) is a thin-film growth technique that normally includes four stages. First, a pulsed laser is focused onto a target material, and each laser pulse ablates a small amount of the material. Second, the high temperature generated at the target surface causes emission of ions, electrons, neutral atoms and molecules. Further irradiation by the laser ionises these species and forms a plasma above the target surface. Third, the ablated material is ejected from the target and moves towards the substrate, forming a plasma plume. Finally, matter reaches the substrate, nucleates, and grows to films. A schematic diagram of a pulsed laser deposition system is shown in Figure 2.1.

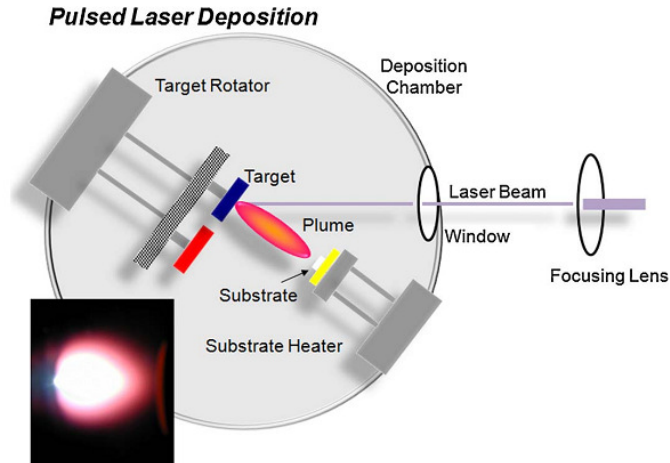


Figure 2.1 Schematic diagram of the pulsed laser deposition (PLD) system.

(Reproduced from [58])

PLD is widely used for complex oxide film growth as it has some advantages which include the following:

- Transfer of stoichiometry from target to film. As when the laser fluence exceeds an ablation threshold that depends on the absorption coefficient of the material, all of the constituent elements of the target are ablated, resulting in vaporization that is independent of the vapor pressures of the constituent elements [57].
- A high energy plume is produced, since the plasma absorbs the laser radiation, resulting in further heating of the plasma. Plasma temperature is up to 3000-5000K, and the kinetic energy of individual ions in a plume can exceed 100 eV. Even when ablated species reach substrates at relatively low temperature, they still have sufficient energy to move and form a dense film [57].
- There is no electron beam or hot filament in the deposition chamber, and the laser is located outside the chamber, so the reactive deposition with ambient gases can be performed. For example, oxides can be grown by introducing reactive gases such as O_2 into the deposition chamber at high pressure. It is

therefore possible to deposit materials at high pressures and temperatures. It is not possible in any other vacuum deposition process [57].

PLD has some drawbacks which include the following:

- Particulates with the diameter in the 0.1 μm to 10 μm range appear in the PLD thin films. The large particulates are produced in two ways. First, irregular fragments are blown off the target. Second, round, solidified droplets are formed from subsurface superheating and melting of the target, and then molten droplets can be ejected from the target by laser beam. On the other hand, smaller particulates 1-100nm in diameter can also be produced from the condensation from ablated vapor species [57].
- A point ablation source produces an angular distribution of plume $f(\theta)$, as shown in Figure 2.2, given approximately by $\cos^n\theta$, where θ is the angle of ejection of material, measured from the normal to the target surface. In the case of PLD, the value of n is in the range from 4 to 25. Consequently uniform-thickness films would be produced only in a narrow angular range [57].

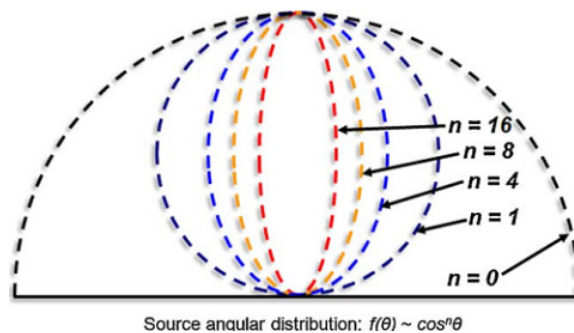


Figure 2.2 Schematic illustration of the shape of a plasma plume created by pulsed laser deposition. The angular distribution of the plume is dominated by a $\cos^n\theta$ function. (Reproduced from [58])

In this research, BiMnO₃ thin films were deposited using a KrF excimer gas laser (Compex 201, Lambda Physik) with a wavelength of 248 nm and pulse duration of around 8 ns.

2.1.1 The Effect of Laser Fluence

High laser fluence leads to the stoichiometric transfer, but can produce particulates on thin films. Use of a relatively low laser fluence can significantly reduce the particulate count, but low laser fluence reduces the deposition rate, and too-low laser fluence results in nonstoichiometric transfer [57].

2.1.2 The Effect of Background Gas

The use of background gas can control film composition or doping, and simultaneously moderate the ablation beam's kinetic energy via gas-phase collisions. At sufficiently high pressures, gas-phase collisions completely thermalize the initial kinetic energy of ablated atoms/ions so that it is not delivered to the growing film surface. Also, at high deposition temperatures, oxide materials tend to lose oxygen. Thus, to compensate this loss, depositions are typically performed in an excess of oxygen [57].

2.1.3 The Effect of Target-Substrate Separation

Higher energy ions and atoms can cause damage if the pressure is too low or the substrate too close to the target. On the other hand, if the substrate is too far away or the pressure too high, the incident atoms and ions are fully thermalized by collisions and do not contribute sufficiently to surface bond-breaking or to activate diffusion [57].

2.1.4 The Effect of Growth Temperatures

Bonds can be broken and incident atoms can diffuse on the growing surface using only thermal energy. For example, high-quality YBCO films can be grown at temperatures of 750-800°C for a broad range of oxygen pressures [57].

2.2 Preparation of PLD Targets of BiMnO₃

To fabricate a ceramic target with a size suitable for the pulsed laser deposition system (20 mm in diameter and 5 mm in height), 10 g powder mixture of Bi₂O₃ and Mn₂O₃ was used for each target preparation. The raw powder materials Bi₂O₃ (99.999% purity) and Mn₂O₃ (99% purity) were purchased from Sigma-Aldrich. Due to the high volatility of bismuth during the deposition process, Bi-rich targets were used in the deposition process [38, 39, 40]. Hence, the amounts of Bi₂O₃ and Mn₂O₃ were calculated and weighed to ensure that the powder mixture had the molar ratio of bismuth to manganese of 1.2. The two powders were mixed and ball milled in isopropanol for 24 hours. After ball milling, the slurry was collected in a 250 ml beaker and heated at 70°C using a hot plate to evaporate the solvent. The dry mixture was placed in an alumina crucible and fired at 700°C for 24 hours to remove organic materials. The resulting powder was ground with a mortar and a pestle, sieved with a 500- μ m-aperture sieve, and then die-pressed to a disk of 20 mm in diameter and 5 mm in height. Then the disk was placed on an alumina plate and sintered in the air atmosphere at 780 °C for 8 hours to form a dense ceramic target.

2.3 X-ray Diffraction (XRD)

X-rays are a form of electromagnetic radiation with short wavelengths, which are of the same order of magnitude as interatomic spacings range. When an X-ray beam is incident on a solid with a periodic arrangement of atoms, parts of the beam are

scattered in all directions. The principle of X-ray diffraction can be explained as follows. A parallel and monochromatic X-ray beam of wavelength λ is incident to two neighbouring lattice planes having the same Miller indices at an angle θ . The constructive interference of scattered X-rays will occur at an angle θ to this plane, if the path difference which X-rays travel between two neighbouring lattice planes is equal to an integral multiple of wavelength λ (See Figure 2.3). The condition required to result in constructive interference is known as Bragg's Law given by

$$2d_{hkl} \sin \theta = n\lambda \quad (3.1)$$

where d_{hkl} is the distance between two adjacent planes, θ is the incident angle, n is an integral and λ is the wavelength of incident X-ray. Bragg's law is a necessary condition for X-ray diffraction. If the atoms are only situated on the corners of unit cell, Bragg's law can successfully predict when diffraction occurs [59].

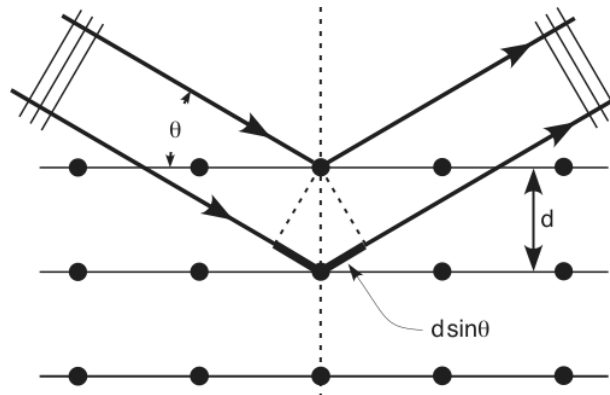


Figure 2.3 Diffraction of x-rays by planes of atoms

However, any atoms lying within the unit cell can be equivalent to additional scattering centers, can produce out-of-phase scattering in certain Bragg angles. The important result is that some diffraction peaks which should exist according to Bragg's law are absent. For example, for BCC crystal structures, the sum of three miller index, h , k , and l , must be even, whereas for FCC, h , k , and l are all either even

or odd. Such phenomenon is known as “systematic absences” [59].

An often-used instrument for measuring the Bragg reflection of a thin film is the $\theta/2\theta$ diffractometer. The working principle of a $\theta/2\theta$ scan mode is as follows. The sample is positioned in the center of the instrument and the probing x-ray beam is directed to the sample surface at an angle θ . At the same angle the detector monitors the scattered radiation. During the scan the angle of the incoming and exiting beam are continuously varied, but they remain equal throughout the whole scan: $\theta_{in} = \theta_{out}$. Due to this geometrical constraint only those lattice planes hkl that are oriented parallel to the surface plane can contribute to a Bragg reflection.

The specimen is rotated about the axis. The monochromatic x-ray beam is generated. The intensities of diffracted beams are detected with a counter. The sample is rotated by θ and the counter is rotated by 2θ so that the incident and reflection angles are maintained equal to one another. As the counter moves at constant angular velocity, a recorder automatically plots the diffracted beam intensity as a function of 2θ . Therefore, the diffraction patterns of the unknown materials are obtained with a diffractometer.

One of the primary uses of X-ray diffractometry is for the determination of crystal structure. Any one diffraction pattern is characterized by a set of “line positions 2θ ” and a set of “relative line intensities I ”. The shape and size of the unit cell are deduced from the angular positions of the diffraction lines of an “indexed pattern”, where a specific crystal system has been assumed and correct Miller indices have been assigned to each reflection. The number of atoms per unit cell is then computed from the shape and size of the unit cell, the chemical composition of the specimen, and its

measured density. The positions of the atoms within the unit cell are deduced from the relative intensities of the diffraction lines. The determination of an unknown structure is quite difficult and complex.

Other uses of x-rays include qualitative chemical identifications. The identification of chemical phases thus proceeds by comparing the measured diffraction patterns with a series of possible patterns covered in Powder Diffraction File (PDF) published by International Centre for Diffraction Data (ICDD).

The diffraction patterns of bulk PLD targets were obtained using a PANalytical X'Pert powder diffractometer equipped with a nickel filter and Cu K_{α} radiation (K_{α} (weighted average)= 1.5418Å) operated at 40kV and 40mA. Digital data were collected only in the θ/θ scan mode, where during the measurement the specimen is always supported horizontally and rotated, and the incident and diffracted X-ray beams both form the same angle θ to the surface of a flat sample (See Figure 2.4).

However, a conventional $\theta/2\theta$ or θ/θ measurement could only obtain the information on the out-of-plane orientation, rather than the in-plane orientation, so the characterization of thin films was performed using a Philips X'Pert PRO MRD Diffractometer with a nickel filter and stationary Cu K_{α} source (K_{α} (weighted average)= 1.5418Å) operated at 40kV and 40mA, as schematically illustrated in Figure 2.5, where the diffractometer has an incident angle of ω , a scattering angle of 2θ , a rotation about the film surface normal of φ and an inclination perpendicular to the scattering plane of ψ .

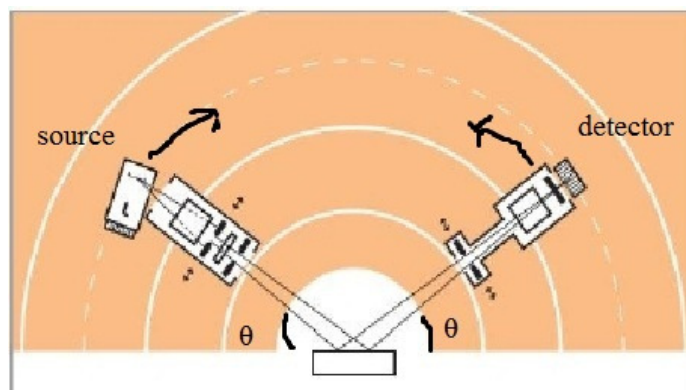


Figure 2.4 Schematic diagram of PANalytical X'Pert powder diffractometer (front view) (Reproduced from [60])

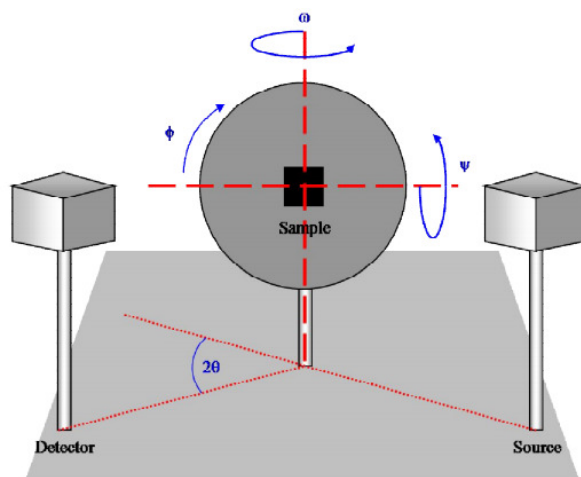


Figure 2.5 Schematic diagram of a Philips X'Pert PRO MRD Diffractometer, showing the 2θ , ω , ϕ and Ψ scan axes. (Reproduced from [61])

For the X-ray diffraction of the thin films, the data were collected in $2\theta/\omega$ scan mode, This type of scan is known as “ $2\theta/\omega$ scan”, because it couples the 2θ rotation of the detector around the sample and the ω rotation of the sample around the same axis. Furthermore, the condition of $\omega = 2\theta/2$ was set. In addition to $2\theta/\omega$ scan, phi (ϕ) scan was also carried out to obtain the information on “plane rotation symmetry” of films and substrate, further determining the epitaxy and in-plane orientation of the film. For ϕ scan, the positions of the incident and diffracted x-ray beams are fixed, so the

detector was first fixed to a certain position, and the crystal tilted about the Ψ scan axis, so that the detector was oriented toward any plane not parallel to the preferred plane of the crystal, and then the crystal rotates about its surface normal, namely the φ axis. In this study, SrTiO₃ has a cubic unit cell, so the interplanar angle required for tilting the crystal is given by the following equation [59]

$$\cos \Psi = \frac{h_1 h_2 + k_1 k_2 + l_1 l_2}{\sqrt{(h_1^2 + k_1^2 + l_1^2)(h_2^2 + k_2^2 + l_2^2)}}$$

SrTiO₃ has several lattice planes that are suitable, such as (100), (110) and (111). Among them, SrTiO₃ (110) plane was randomly chosen to orient toward the detector in φ scan. BiMnO₃ has a monoclinic unit cell, so the interplanar angle required for tilting the crystal is given by the following equation [59]

$$\cos \Psi = \frac{d_1 d_2}{\sin^2 \beta} \left[\frac{h_1 h_2}{a^2} + \frac{k_1 k_2 \sin^2 \beta}{b^2} + \frac{l_1 l_2}{c^2} - \frac{(l_1 h_2 + l_2 h_1) \cos \beta}{ac} \right]$$

where a, b, c are the lattice parameters of the unit cell, and $\alpha, \beta,$ and γ are the angles between them. BiMnO₃ have several lattice planes that are suitable, such as (020), (110), (202), and (400). Among them, BiMnO₃ (400) plane was randomly chosen to orient toward the detector in the φ scan.

2.4 Scanning Electron Microscopy (SEM)

A JEOL6400 JSM6400 SEM was used to observe the microstructure of PLD targets. The sample chamber of the instrument is illustrated in Figure 2.6, where an electron beam is generated by an electron gun at the top. This beam is focused by two magnetic lenses inside the column and hits the sample in a very small spot.

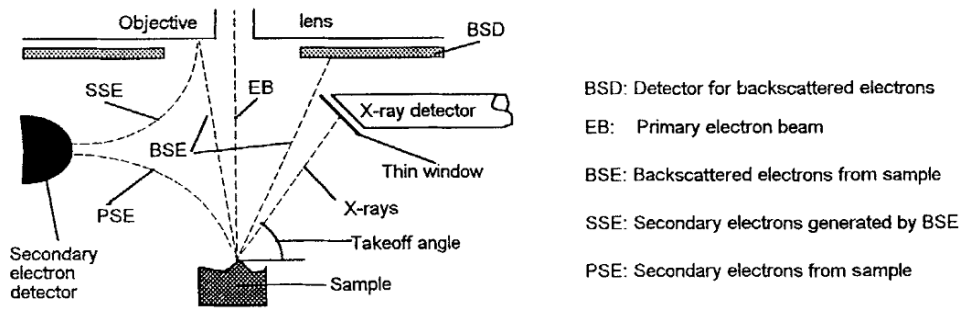


Fig.2.6 Schematic diagram of scanning electron microscopy (Reproduced from [62])

Consider the interaction between the electron beam and specimen first. The bombardment of electrons on solid materials produces the emission of secondary electrons, back scattering electrons, Auger electrons, characteristic X-ray, cathodoluminescence, etc. The detection of secondary electrons and back scattering electrons is used in scanning electron microscopy [62].

When electron beams hit the atoms in the solid, some weak bonding electrons are ejected from the surface; they are known as secondary electrons with energy less than 50 eV. Since they are low energy electrons, only secondary electrons within the depth of 50-500 Å can be detected. Hence, the number of resulting secondary electrons strongly depends on the sample topography and can be used for surface characterization.

Backscattered electrons are generated when the incident electron beam collides elastically with the sample atoms; the scattered electrons present energies close to the primary beam energy. The backscattered electrons are generated at around 5000 Å in depth. The number of backscattered electrons is determined by the types of elements. With the Back-Scattered Electron (BSE) signal, one can observe the distribution of

the mean atomic number of the sample; bright regions are associated with heavy elements in that area.

Scanning electron microscopy with Energy Dispersive spectrometry (EDS) can be used to carry out the quantitative analysis of the ceramic target. X-ray spectra are collected as a number of counts within an energy range for a certain acquisition time. An X-ray spectrum is usually displayed as a function of energy. It consists of a continuous signal with superimposed characteristic elemental lines. The positions of the elemental lines are related to the atomic number of the elements generating them. True atomic composition in sample can be determined by a series of calculations involves observed X-ray intensity ratios.

EDS point analysis on the identical phases in BES images was made three times, and the data were treated by introducing the concept of errors. The results were expressed as “ $\bar{x} \pm \sigma_m$ ”, where \bar{x} is mean value and σ_m is standard deviation. (See Appendix A for more details on standard deviation)

2.5 Density Measurement of PLD Targets

The density of the PLD targets was determined using a specifically designed microbalance (Sartorius YDK01 Density Determination Kit, Sartorius AG) by means of the Archimedean principle [63], as shown below

$$\rho = \frac{W(a) \cdot \rho(fl)}{W(a) - W(fl)}$$

where ρ is the density of the specimen, $W(a)$ is the weight of the specimen in air, $W(fl)$

is the weight of the specimen in liquid, $\rho(\text{fl})$ is the density of the liquid. Prior to measuring $W(\text{fl})$, the target was immersed in distilled water in a beaker, and then the beaker was placed in a vacuum environment for 15 minutes to exclude the weight of gases in the external voids of the samples.

The theoretical density of the sample can be determined by the formula:

$$\rho_{\text{theoretical}} = \frac{\text{mass of ions within unit cell}}{\text{volume of unit cell}} = \frac{n'(\sum M_A + \sum M_B)}{V_C N_A}$$

where n' is the number of cation and anion atoms in the unit cell, $\sum M_A$ is the sum of atomic weights of all cations in the unit cell, $\sum M_B$ is the sum of atomic weights of all anions in the unit cell, V_C is the volume of unit cell, and N_A is Avogadro constant (i.e. $6.022 \times 10^{23} \text{ mol}^{-1}$). The related lattice parameters of materials can be obtained from crystallographic data, that is, Inorganic Crystal Structure Database (ICSD) from Chemical Database Service (CDS). The PLD target must have a measured density, higher than 80% of the theoretical density.

2.6 Thickness Measurement of Thin Films

The film thickness was measured using a Veeco Dektak 150 stylus surface profiler capable of providing a vertical resolution of 0.1 nm [64]. During the measurement, the stylus exerts a constant force on the sample to be measured. When the stylus is dragged across a surface step, a piezoelectric crystal sends out a signal that is proportional to the height of the step. To create such a step, prior to the deposition of BiMnO_3 , one corner of each SrTiO_3 substrate was covered with a droplet of TiO_2 paint. After the deposition, the sample was ultrasonically cleaned with acetone,

isopropanol and distilled water respectively for 3 minutes. During these cleaning processes, the TiO_2 paint covering the SrTiO_3 substrate was removed, and then created a step between the film and the substrate. Thus, the film thickness could be determined by measuring the height of the step.

2.7 Magnetic Measurement by PPMS

Magnetic measurements were performed using a commercial Physical Properties Measurement System (PPMS) from Quantum Design [65]. PPMS is a versatile instrument capable of measuring physical properties of samples such as electrical resistivity, magnetization, hall effect, heat capacity, and thermal conductivity. The PPMS contains a rod-like probe equipped with a 7 Tesla longitudinal superconducting magnet and a temperature controller in the range 2K to 350K (See Figure 2.7). The probe is the component that is inserted into the dewar. The probe is composed of several concentric stainless steel tubes and other important elements. Its outer layer isolates the sample chamber from the liquid-helium bath. The magnet is a superconducting solenoid composed of a niobium–titanium alloy embedded in copper. It is on the outside of the probe, so it is always immersed in liquid helium. The magnet coil constitutes a closed superconducting circuit. When the heater is turned off, the entire magnet can superconduct, which eliminates the need for a current source during constant magnetic field operation.

The Vibrating Sample Magnetometer (VSM) option of the PPMS is a fast and sensitive DC magnetometer. The basic principle of measurement for a vibrating sample magnetometer is based on Faraday's law of induction, namely that an induced electromotive force (emf) is induced in the loop when the number of magnetic field lines that pass through the loop is changing. Figure 2.8 shows system components for

PPMS VSM option. To performed VSM measurements, the coilset puck which contained the VSM detection coils and a thermometer for monitoring the sample temperature was inserted into the sample chamber. The sample was attached to the end of a sample rod, and the sample rod was inserted the bore of the coilset in the sample chamber. The linear motor transport which could move the sample was installed directly on top of the PPMS sample-chamber opening. During the measurement, the sample was oscillated near a detection (pickup) coil, producing a changing magnetic flux. The voltage in a pickup coil induced by a changing magnetic flux was synchronously detected.

The two types of DC magnetic measurement were carried out to characterize magnetic materials: magnetization versus field (M-H) measurement and magnetization versus temperature (M-T) measurement. First, the magnetization versus field (M-H) curve measurement shows the saturation magnetization (M_S), remanent magnetization (M_r), and coercive field (H_C). Second, magnetization versus temperature measurements is usually done by taking zero field cooled (ZFC) and field cooled (FC) magnetization curves [66].

In the zero field cooled (ZFC) mode, the sample was cooled with field = 0 to low temperature, so that the magnetic moments of the particles had random orientations, and then a small constant field was applied so that there was a measurable magnetization as the temperature was increased. The magnetization as a function of temperature was collected in the “warming” process. In the field cooled (FC) mode, a field was first applied to the sample at room temperature, and the sample was cooled to the low temperature in the field. The temperature dependence of magnetization was recorded in the “cooling” process.

All the magnetization data needed to be treated by a process called “normalizing”. The signal from the sample is proportional to the amount of material. Therefore, to compare results to theory or measurements done elsewhere, one needs to know how much signal per sample volume or mass or number of atoms, etc. Because one knows the film area (equal to substrate area), one can calculate the film volume if the film thickness is known. You want to know how many Bohr magneton (μ_B) you measure per Mn ion and see whether it is a reasonable value.

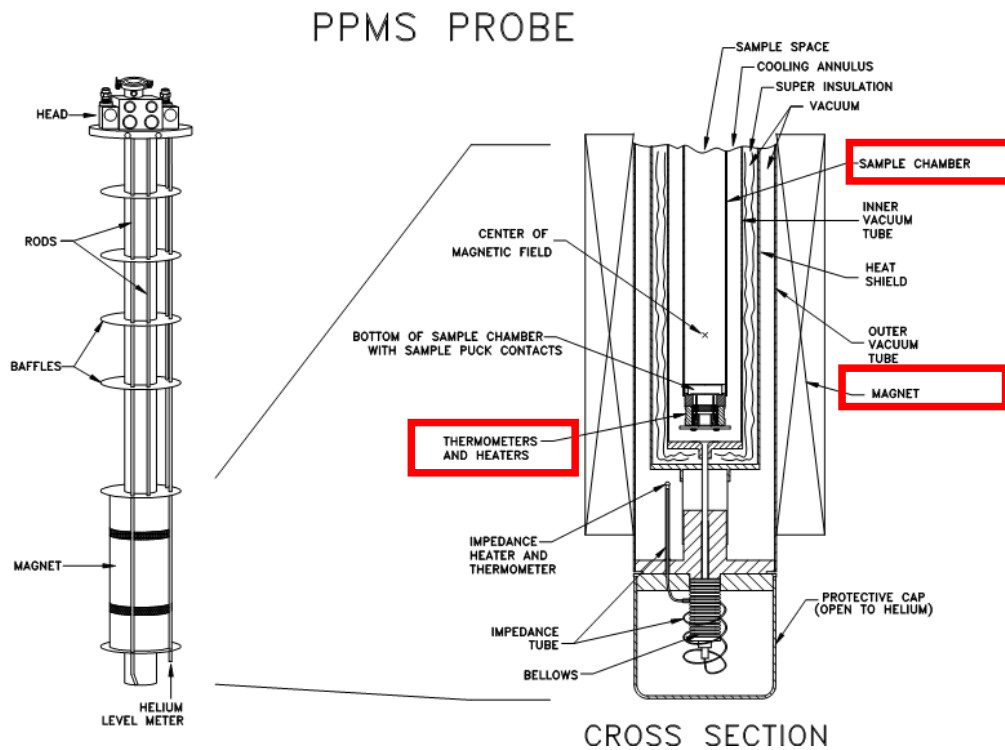


Figure 2.7 Schematic diagram of PPMS probe showing major components

(Reproduced from [65])

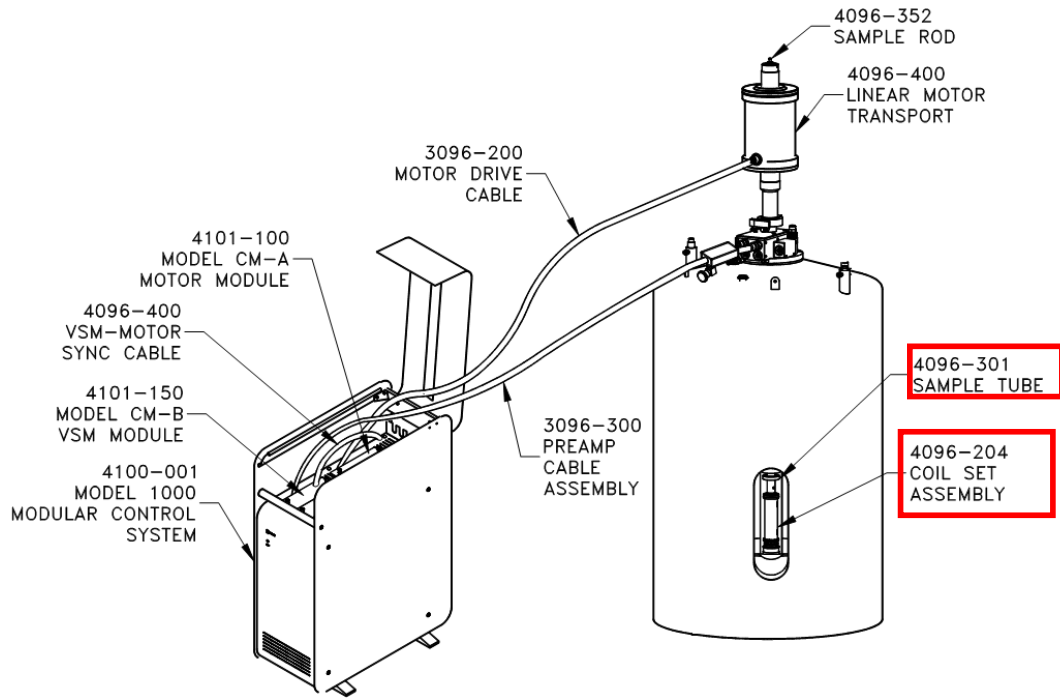


Figure 2.8 Schematic diagram of system components for PPMS VSM option

(Reproduced from [65])

Chapter 3 Result and Discussion

3.1 Characterization of $\text{Bi}_{1.2}\text{MnO}_3$ Target

3.1.1 Qualitative Compositional Analysis

Figure 3.1 shows a θ - 2θ scan of an as-prepared $\text{Bi}_{1.2}\text{MnO}_3$ target, demonstrating the existence of two different phases, $\text{Bi}_2\text{Mn}_4\text{O}_9$ and Bi_2O_3 , in the sample, which is consistent with results reported by other groups [37]. Figure 3.2 shows SEM images of the target, confirming that the sample is multiphase. The back scattered electron image shows two different phases are present; the bright regions are associated with heavy elements in that area, while the dark regions correspond to the phase with lighter atomic number.

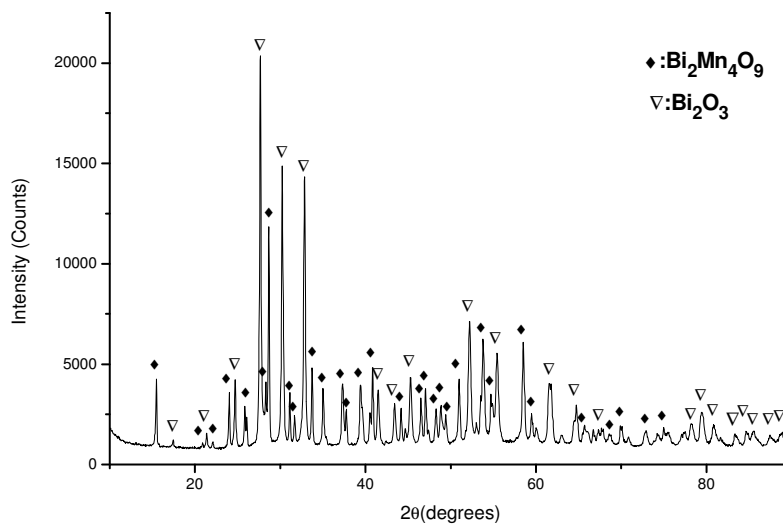


Figure 3.1 θ/θ diffraction pattern for the nominal $\text{Bi}_{1.2}\text{MnO}_3$ target

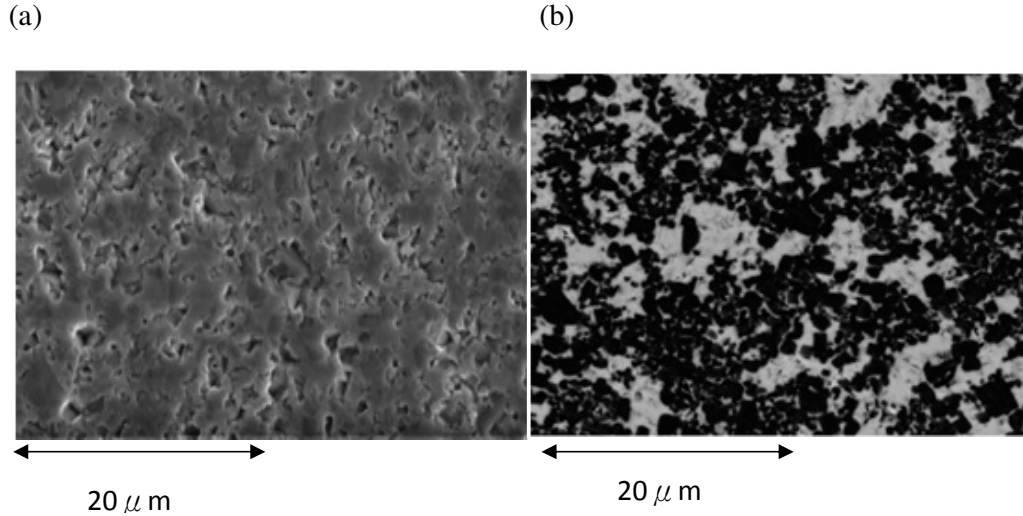


Figure 3.2 Scanning electron micrographs of the nominal $\text{Bi}_{1.2}\text{MnO}_3$ target (a) secondary-electron image (b) backscattered electron image.

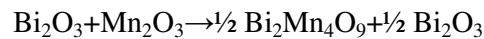
In Table 3.1, the quantitative EDS-analysis of the target implied that bright and dark regions correspond to $\text{Bi}_2\text{Mn}_4\text{O}_9$ and Bi_2O_3 , respectively. In addition, the measured overall Bi:Mn atomic ratio was 1.2:1, which was in agreement with the composition ratio intended for the target, implying elemental loss did not occur during the calcinations or sintering. During pulsed laser deposition, the laser struck the rotating target at an angle. A target which was homogeneous in composition was desired so that the laser could simultaneously ablate these two phases Bi_2O_3 and $\text{Bi}_2\text{Mn}_4\text{O}_9$. As shown in Figure 3.2(b), both phases can be seen to have the lateral dimensions around $5\text{-}10\ \mu\text{m}$ which are much smaller than the laser beam spot size ($0.2\ \text{cm}^2$). The compositional analysis confirmed that the solid state synthesis achieve the correct cation ratio in the target.

Area	Atomic% Mn	Atomic% Bi	Atomic% O
Bright regions	26.56±2.11	13.20±1.56	59.01±1.74
Dark regions	0.72±1.56	39.52±2.09	58.35±1.86
Overall	20.33±1.63	23.98±1.77	55.99±1.43

Table 3.1 EDS analysis of the nominal Bi_{1.2}MnO₃ target

3.1.2 Density Determination

By using the Archimedean principle, the Bi_{1.2}MnO₃ target was found to have a density of 7.71 g/cm³. From the combination of XRD (Fig 4.1) and EDS analysis (Fig 4.2), the target consists of two phases, including Bi₂Mn₄O₉ and Bi₂O₃. Since the presence of Mn₂O₃ phase was not observed in the target, the solid state synthesis reaction



was considered to be a complete reaction after the 24 hour calcinations and the 8 hour sintering, namely that 1.2 mole of Bi₂O₃ reacted with 1 mole of Mn₂O₃ to form 0.5 mole of Bi₂Mn₄O₉ and 0.7 mole of Bi₂O₃.

From the data obtained from the Inorganic Crystal Structure Database (ICSD), Bi₂O₃ and Bi₂Mn₄O₉ were calculated to have theoretical densities of 9.34 g/cm³ and 7.14 g/cm³, respectively. Hence, an ideal dual-phase sample with the Bi₂O₃:Bi₂Mn₄O₉ ratio of 7/5 should have a theoretical density of 8.42 g/cm³. By comparing the actual density and the theoretical density, it was proposed that the target prepared has a 91.5% of the theoretical density, which was higher than the minimum requirement of the 80% required for PLD [67].

3.2 Thin Film Deposition

3.2.1 Selection of Deposition Parameters

BiMnO₃ thin films were produced using PLD. The growth of thin films involved a number of process variables including target–substrate separation, background gas pressure, laser spot size, and laser energy density, etc [57]. In most cases, BiMnO₃ thin films were grown at the temperature range between 700°C and 600°C, however, Eerenstein et al. have reported the deposition of BiMnO₃ at relatively low temperature and pressure [39]. Since the PLD system used could not provide a precise control over the value of oxygen supply, we grew BiMnO₃ thin films in the temperature range of 600°C to 700°C.

According to the literature [38, 39, 40], the growth of BiMnO₃ was extremely sensitive to the substrate deposition temperature, so the effect of substrate deposition temperature on film structures was the first variable to be studied. The oxygen pressure was chosen to be 75mTorr, the same as used by Moreira dos Santos et al [38]. The distance between the target and substrate, fluence, and repetition rate were fixed to be 5 cm, 520 mJ, and 8 Hz, respectively. In terms of the cooling process, the films were cooled at the system's fastest cooling rate (50°C/min) in 7.6×10^5 mTorr of oxygen to prevent Bi evaporation. Table 3.2 summarizes the PLD parameters that were studied during the course of this investigation.

No	Target	Substrate Temp. (°C)	Oxygen pressure (mTorr)	Cooling rate (°C/min)	Post annealing	XRD
1	Bi _{1.2} MnO ₃	600	75	50	None	Figure 3.3(f)
2	Bi _{1.2} MnO ₃	650	75	50	None	Figure 3.3(b)
3	Bi _{1.2} MnO ₃	700	75	50	None	Figure 3.3(a)
4	Bi _{1.2} MnO ₃	625	75	50	None	Figure 3.3(e)
5	Bi _{1.2} MnO ₃	630	75	50	None	Figure 3.3(d)
6	Bi _{1.2} MnO ₃	640	75	50	None	Figure 3.3(c)
7	Bi _{1.2} MnO ₃	640	20	50	None	Figure 3.4(c)
8	Bi _{1.2} MnO ₃	640	100	50	None	Figure 3.4(a)
9	Bi _{1.2} MnO ₃	640	75	50	550°C 20 mins	Figure 3.5(a)

Table 3.2: A listing of the PLD parameters that were studied. Note: laser fluence (520mJ on a spot size of $0.2\text{cm}^2 = 2.6\text{J}/\text{cm}^2$), repetition rate (8Hz), and target-substrate distance (5cm) were fixed for all deposition.

3.3 Structural Characterization of BiMnO₃ Films on SrTiO₃ Substrate

This section described the characterization of the microstructure and composition of the prepared thin films to confirm whether single phase epitaxial BiMnO₃ thin films were grown. Structural studies were carried out using XRD. Compositional analyses were conducted using EDS.

3.3.1 The Effect of Substrate Deposition Temperature

XRD analyses of the thin films grown at a range of temperatures from 600°C to 700°C were performed, as shown in Figure 3.3. For temperatures in the range from 650°C to 700°C, the deposited thin films exhibited an excess of manganese (Figure 3.3(a) and 3.3(b)). In addition to BiMnO₃, the presence of other Mn-rich phases, such as MnO₂ and Mn₅O₇, were observed in the film grown at 650°C. The MnO₂ phase grew with (200) orientation. For temperatures below 630°C, the films contained Bi-rich phases, including Bi₂O₄ and Bi₂O_{2.33}, and some unidentified phases. Although the starting material was Bi₂O₃, Bi₂O₄ and Bi₂O_{2.33} both occurred possibly due to epitaxial stabilization. The observed aluminum peak resulted from the sample holder of the X-ray diffractometer.

The thin film grown at 640°C (Figure 3.3c) seemed single phase, and only one weak diffraction peak was present around 71°. By comparing peak positions and relative peak intensities using the Inorganic Crystal Structure Database (ICSD), the XRD pattern of the thin film grown at 640°C was qualitatively determined to be single phase (-202)-oriented BiMnO₃ (ICSD code: 245299) [BiMnO₃(-202) || SrTiO₃(100)]. From the data of BiMnO₃ and SrTiO₃ in the ICSD, the diffraction peaks produced by (-202)-oriented BiMnO₃ could be identified at the 2θ positions of 22.29°, 45.50° and 70.91°, all of which lie very close to the peaks produced by (100)-oriented SrTiO₃, located at 2θ of 22.78°, 46.48° and 72.54°. Thus, there was an overlap between the diffraction peaks of the two materials, especially at low diffraction angles, so the position differences might be less than the best available resolution of the X-ray diffractometer used and hence not distinguishable.

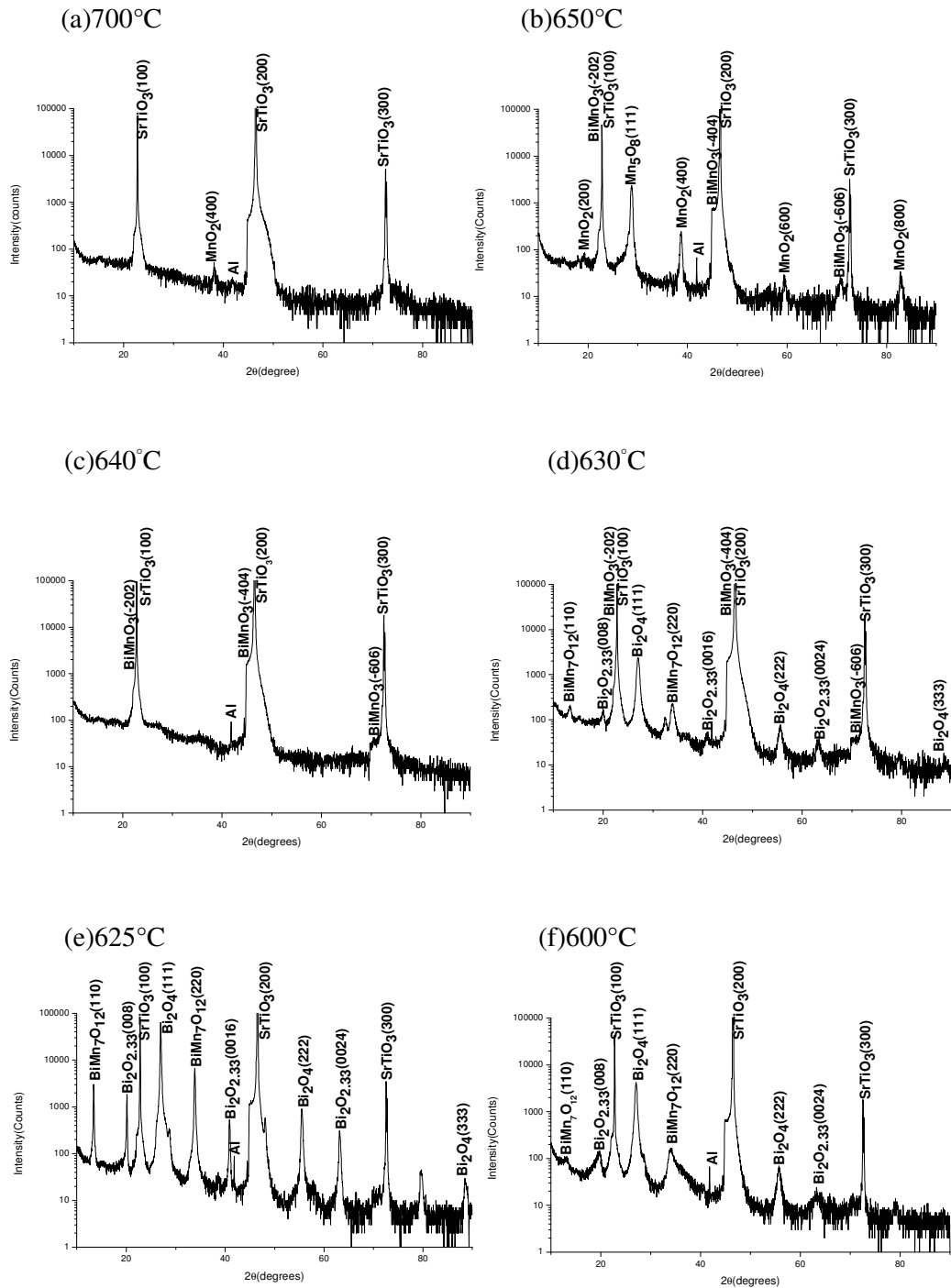


Figure 3.3 diffraction patterns for BiMnO₃ thin films grown with the Bi_{1.2}MnO₃ target at the temperatures of (a) 700 °C, (b) 650 °C, (c) 640 °C, (d) 630 °C, (e) 625 °C, and (f) 600°C in an oxygen pressure of 75 mTorr. See No.1-6 in Table 3.2 for corresponding growth conditions.

From the diffraction patterns for 640°C and 650°C, it was observed that the rise in the temperature improved the crystallinity of the BiMnO₃ phases, but it also facilitated the volatility of bismuth, leading to further enriching in Mn-rich phases. Clearly, the change in the substrate deposition temperatures would influence the volatility of bismuth significantly. In order to grow single phase BiMnO₃ thin films with a Bi:Mn ratio 1:1, when using a Bi-rich target, it is important to adjust the substrate deposition temperatures to control the adsorption and evaporation of bismuth atoms. It was argued that the films grown from the target with the nominal composition of Bi_{1.2}MnO₃ at the substrate deposition temperature of 640°C in an oxygen pressure of 75 mTorr are (-202)-oriented BiMnO₃.

The chemical composition of several thin films was studied using EDS, as shown in Table 3.3. It was obvious to see that the film grown at 700 °C is deficient in bismuth. By comparing the Bi:Mn ratios of films grown at 640 and 650 °C, it was found that the film grown at 640°C contained a larger Bi:Mn ratio than those were grown at 650 °C, despite the observation of only BiMnO₃ in the XRD pattern (see Figure 3.3(c)). The film grown at 650°C is also Mn-rich, which was in agreement with the XRD pattern of Figure 3.3(b).

The thicknesses of deposited films were measured using a Dektak 150 stylus surface profiler. Table 3.4 shows the relationship between film thicknesses and substrate deposition temperatures. Clearly, there was no significant difference in thickness between the films grown at different temperatures due to the set of fixed laser pulses, fluence and substrate-target distance.

	Grown at 640 °C	Grown at 650 °C	Grown at 700 °C
Element	Atomic (%)	Atomic (%)	Atomic (%)
Sr	48.93± 0.88	48.74± 0.73	50.61± 0.88
Ti	48.81± 0.76	48.6± 0.97	48.76± 0.87
Bi	1.05± 0.36	1.17± 0.40	0.44± 0.15
Mn	1.21± 0.41	1.49± 0.50	0.19± 0.64

Table 3.3 EDS results for the films grown at 640 °C, 650 °C, and 700 °C.

Substrate Deposition Temperature (°C)	Film Thickness (nm)
700	45.3± 2.3
650	50.0± 2.7
600	47.6± 2.4

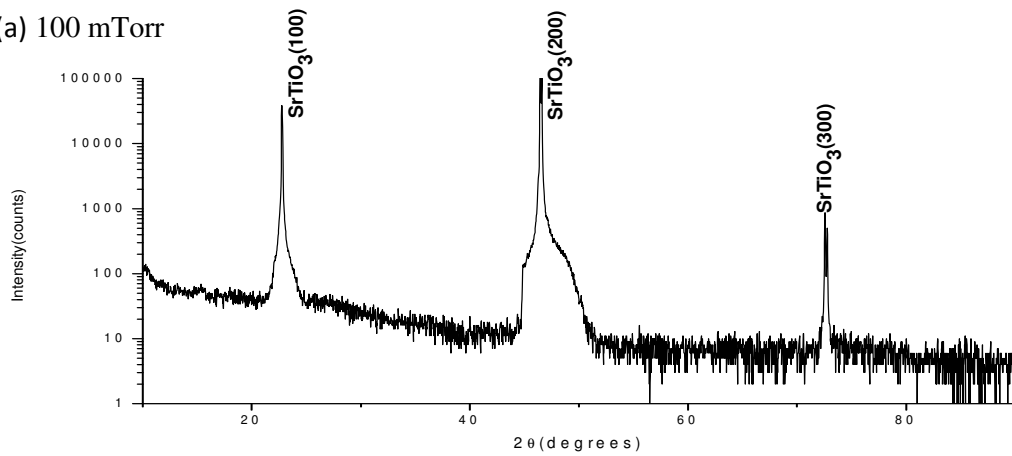
Table 3.4 Film thicknesses corresponding to substrate deposition temperatures

3.3.2 The Effect of Oxygen Pressure

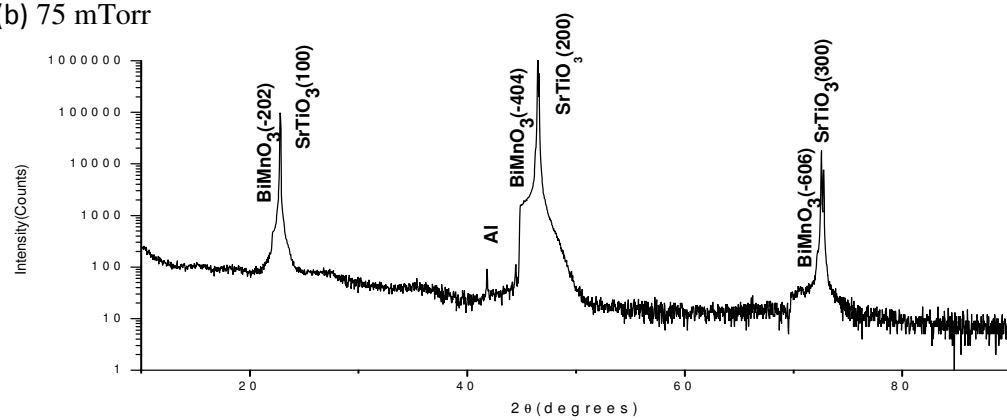
Figure 3.4 shows the X-ray diffraction patterns for the thin films grown at 640 °C in different oxygen pressures (100, 75, and 20 mTorr). It is obvious that the diffraction pattern for 20 mTorr (Fig. 3.4(c)) is similar to the diffraction pattern shown in Fig 3.3(a), indicating the presence of excess Mn. However, for the growth condition at an oxygen pressure of 100 mTorr, the film seemed to be amorphous (Fig 3.4(a)). Both figures suggested that a Mn-rich phase was formed due to the evaporation of bismuth if the pulsed laser deposition is carried out at low oxygen pressure. However, the film crystallinity was not optimal either if the oxygen pressure was too high, since the high background gas pressure could reduce the kinetic energies of the ablated species, as described in other textbooks [57]. Interestingly, the obtained growth condition of 640

°C and 75mTorr seemed to be able to achieve nearly single phase and crystalline BiMnO₃ thin films.

(a) 100 mTorr



(b) 75 mTorr



(c) 20 mTorr

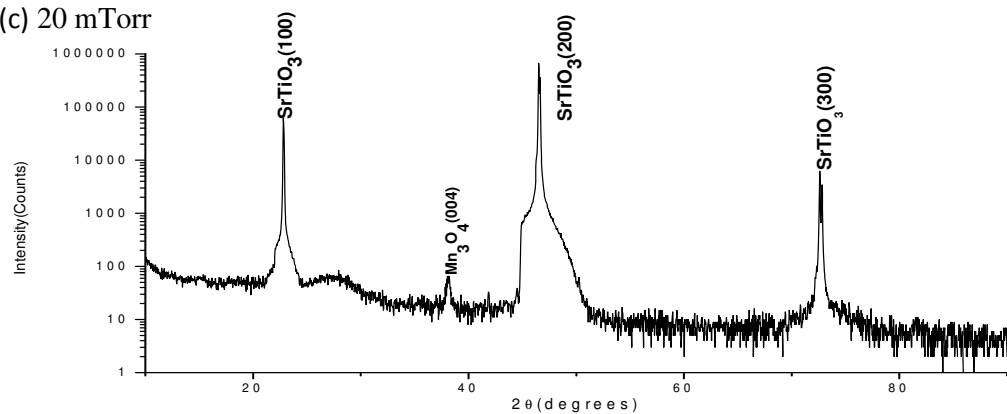


Figure 3.4 diffraction patterns for BiMnO₃ thin films grown with the Bi_{1.2}MnO₃ target at 640 °C in oxygen pressures of (a) 100, (b) 75 and (c) 20 mTorr. See No.6-8 in Table 3.2 for corresponding growth conditions.

3.3.3 The Effect of Post Annealing

The intensity of a diffraction line is proportional to the number of lattice planes contributing to the same reflection, and thus the degree of periodic arrangement of atoms [59]. In order to improve the crystallinity of the film grown at the condition of 640°C and 75mTorr, which could help the qualitative chemical identification, a post annealing treatment was decided to be carried out. After the deposition, the film was cooled down to 550°C at a cooling rate of 50°C/min, dwelled for 20 minutes, and then cooled down to room temperature. Figure 3.5(a) shows the XRD pattern for the sample subject to the post annealing process, revealing that the film clearly had (-202) oriented BiMnO₃, along with small amount of amorphous Mn₅O₈ and some unidentified phases.

A detailed XRD investigation of a film yielded only (-202) peaks for the BMO film corresponding to an out-of-plane lattice parameter of 1.955 Å. The XRD pattern means that this film grown at the condition of 640°C and 75mTorr still requires optimization to remove small amount of amorphous Mn₅O₈. The temperature window for the growth of pure BiMnO₃ is likely to be in the range between 640 and 630°C. It is also possible that the annealing temperature is too high so that certain amount of bismuth is evaporated, further forming Mn₅O₈.

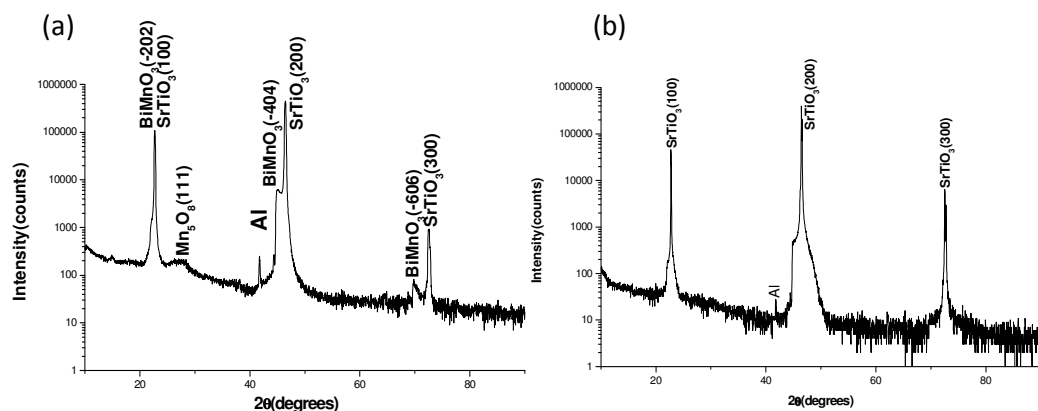


Figure 3.5 diffraction patterns for (a) the sample subjected to the post annealing process and (b) bare SrTiO₃ substrate. See No.9 in Table 3.2 for corresponding growth conditions.

3.4 Determining The Orientation Relationship Between Film and Substrate

Figure 3.6(a) shows the phi scan of the (100)-oriented SrTiO₃ substrate, and the sharp peaks come from (110) reflections. The four sharp peaks spaced 90° apart were located at the 2θ positions of 88°, 178°, 268° and 358°, confirming the four fold rotational symmetry of this SrTiO₃ (100) plane. In addition, the rotational symmetry of the (-202)-oriented BiMnO₃ thin films was examined using (400) reflections, as shown in Figure 3.6(b). The four sharp peaks were found to appear at the 2θ positions of 43°, 133°, 223° and 313°, all of which were spaced 90° apart. Therefore, the (-202) plane of BiMnO₃ also had a four-fold rotational symmetry. It was observed that a 45° rotation between the SrTiO₃ (100) plane and the BiMnO₃ (-202) plane exists.

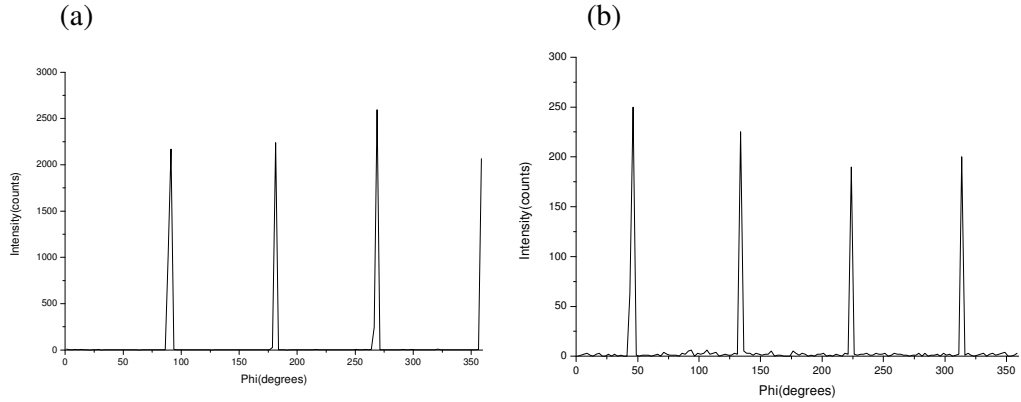


Figure 3.6 Phi scan of (a) the 110 reflection of the (100)-oriented SrTiO₃ substrate ($2\theta = 32.424^\circ$ and $\Psi = 45^\circ$). (b) the 400 reflection of the (-202)-oriented BiMnO₃ film deposited on the (100)-oriented SrTiO₃ substrate ($2\theta = 40.421^\circ$ and $\Psi = 53.96^\circ$).

The epitaxial relation between BiMnO₃ (-202) plane and SrTiO₃ (100) plane could be investigated. First, Figure 3.7 shows the atomic arrangement of SrTiO₃ substrate (100) plane, at which only O and Sr atoms are located. The interatomic distance between each O is 3.905 Å, while that between each Sr is 3.905 Å. Figure 3.8 shows the atomic arrangement of BiMnO₃ (-202) plane, at which only Bi and O atoms are located. The interatomic distance for each Bi is 3.848 Å, while that for each O is 4.519 Å.

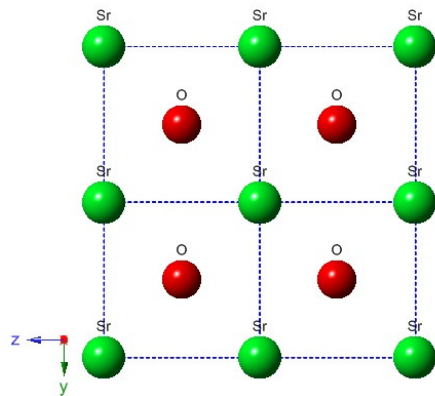


Figure 3.7 Atomic packing of a SrTiO₃ (100) plane

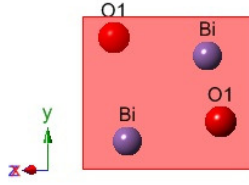


Figure 3.8 Atomic packing of a BiMnO_3 (-202) plane

For film growth by PLD, atoms in the plume come into contact with the substrate surface where they form chemical bonds with atoms in the substrate. Thus, it is necessary to consider the bonding interaction between the atoms of film material and the atoms of substrate. It is known that the strength of a bonding interaction between two different atoms can be measured by the energy required to break the bond, the bond energy [68]. It is also known that Bi and Sr atoms can bond to O atoms to form Bi-O and Sr-O bonds, with bond energies of 343 kJ/mol and 454 kJ/mol, respectively [69]. Bonding interactions between Bi and Sr atoms are negligible. Therefore, BiMnO_3 (-202) plane must rotate by 45° with respect to SrTiO_3 (100) plane (See Figure 3.9) so that Bi and O atoms on BiMnO_3 (-202) plane can bond to O and Sr atoms on SrTiO_3 (100) plane, further leading to Bi-O and Sr-O bonds.

According to the definitions in domain matching epitaxy (DME) [55], in the [010] direction of SrTiO_3 , the initial lattice misfit (-13.58%) between film and substrate in this direction was obtained. In the [001] direction of SrTiO_3 , the initial lattice misfit (1.48%) between film and substrate in this direction was obtained. The epitaxial relation between BiMnO_3 (-202) plane and SrTiO_3 (100) plane is schematically shown in Figure 3.9.

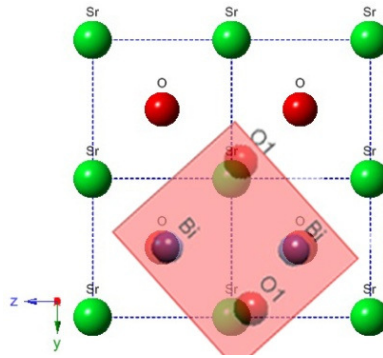


Figure 3.9 Schematic diagram showing the epitaxial relationship of BiMnO₃ (-202) grown on SrTiO₃ (100).

3.5 Magnetic Measurements

Figure 3.10 depicts both zero-field-cooled (ZFC) and field-cooled (FC) magnetic moment (M) versus temperature (T) plots for the BiMnO₃ thin film with an applied field of 100 Oe. The FC magnetization measurement revealed a saturation magnetization of 0.8 μ_B /Mn at 20K, which was lower than the theoretical value of 4.9 μ_B /Mn [36]. The T_c was about 80K, lower than the T_c of 101 K of bulk material [42], probably due to substrate induced strain. The peak at around 50K likely came from artifacts.

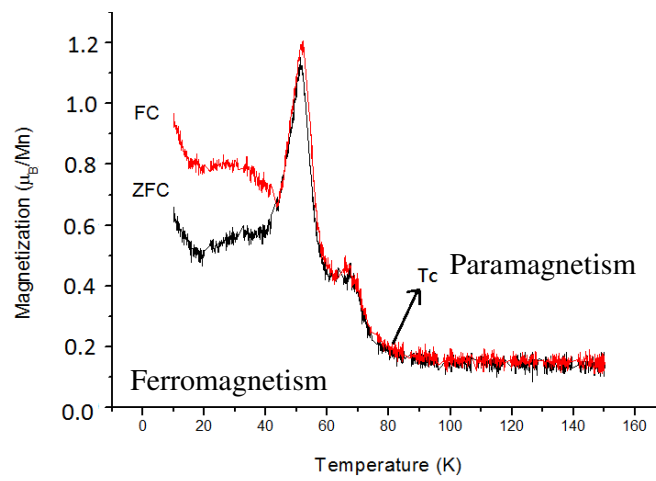


Figure 3.10 ZFC and FC dc-magnetization curves measured as a function of temperature for the BiMnO₃ thin film in a magnetic field of 100 Oe.

For ZFC magnetization curves, before a magnetic field was applied to the sample, the BiMnO₃ was initially at the equilibrium state, where there were a large number of magnetic domains, and all of them might have different magnetization orientations. The magnitude of the net magnetization for the entire solid was the vector sum of the magnetizations of all the domains. Later, a field that was smaller than the anisotropy field was applied, and the magnetization was collected in the warming process. With increasing the temperature from 20K to 45K, the magnetic moments in the domains would turn to the field direction, i.e., the magnetization of samples increased with temperature. At a temperature of around 45K, the magnetization increased to the maximum value. If the temperature increased further, it then decreased, because the thermal energy destroyed the alignment of magnetic moments.

For FC curves, which were performed in the cooling process, the BiMnO₃ thin film was always at the state, where all of the magnetic moments pointed to the field direction. From FC curve, the film has been demonstrated to be a ferromagnet that had spontaneous magnetization. The branching of the ZFC and FC magnetization curves revealed that there was an energy barrier for the flipping of the magnetic moments.

Figure 3.11 shows magnetization vs. magnetic field ($M - H$) plot for the BiMnO₃ film at 20K, showing the hysteresis in the $M - H$ data. The remanent magnetization (M_r) is about 0.2 μ_B/Mn , and the coercive field (H_c) is about 50 (Oe). Both of them are lower than M_r of 0.8 μ_B/Mn and H_c of 300 (Oe) of BiMnO₃ films (laser fluence of 2.2J/cm²) grown by Eerenstein et al. (See Fig 3.11(b)).

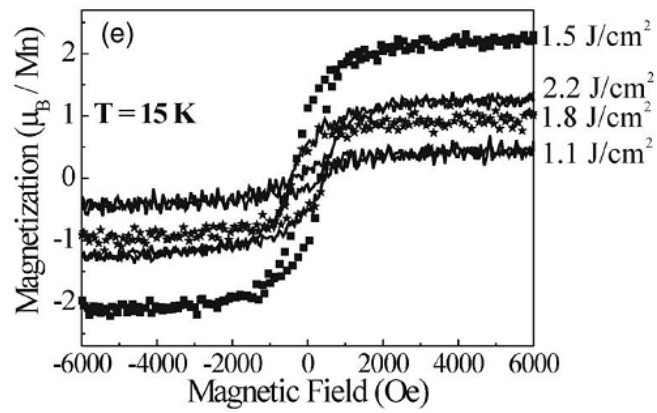
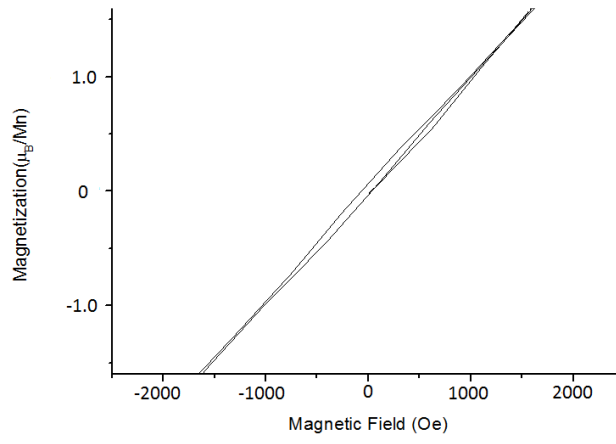


Figure 3.11 Magnetization curves for (a) the prepared BiMnO₃ film at 20K (b) the BiMnO₃ film grown by Eerenstein et al (Reproduced from [39])

Chapter 4 Conclusions and Future Works

Near single-phase BiMnO₃ thin films have been grown on SrTiO₃ (100) substrates by PLD at the temperature of 640°C and an oxygen pressure of 75 mTorr. It appeared that the BiMnO₃ films grew in (-202) orientation. The growth of thin films was extremely sensitive to substrate deposition temperature, and pure phase BiMnO₃ only could be formed in a narrow temperature range. Among all pressures tried, the oxygen pressure of 75 mTorr seemed to be suitable for the growth of BiMnO₃ phase. Also, a post anneal at 550°C effectively improved the crystallinity of the film. The film showed an epitaxial nature which a 45° rotation existed between the SrTiO₃ (100) plane and the BiMnO₃ (-202) plane. Magnetic measurement revealed that the BiMnO₃ film was a ferromagnet with a Curie temperature of about 80K, lower than the bulk material.

In terms of future work, the best growth conditions still need to be researched. The search strategy is that the compositions with the right stoichiometric ratio will be reached at the appropriate substrate deposition temperature, captured at lower temperature using the fastest cooling rate, and then annealed to enhance the crystallinity. Since quite a few articles discuss the temperatures for post annealing for BiMnO₃, the appropriate annealing temperature also needs to be investigated. From the XRD and EDS results, it seems that the best growth temperature should be slightly lower than 640°C. After obtaining high quality single crystal films, the surface roughness should be evaluated using atomic force microscopy (AFM). One could further optimize the deposition process with respect of the surface roughness and electric/ ferroelectric/ magnetic properties.

References

1. K. Rabe, Ch. H. Ahn and J.-M. Triscone, *Physics of ferroelectrics a modern perspective*, Springer 2007.
2. H. Schmid: Multi-ferroic magnetoelectrics, *Ferroelectrics* **162**, 317 (1994).
3. N. A. Spaldin and M. Fiebig: The renaissance of magnetoelectric multiferroics, *Science* **309**, 391 (2005).
4. W. Eerenstein, N. D. Mathur and J. F. Scott: Multiferroic and magnetoelectric materials, *Nature* **442**, 759 (2006).
5. M. Bibes and A. Barthélémy: Multiferroics: Towards a magnetoelectric memory, *Nature Materials* **7**, 425 (2008).
6. J. Wang, J. B. Neaton, H. Zheng, V. Nagarajan, S. B. Ogale, B. Liu, D. Viehland, V. Vaithyanathan, D. G. Schlom, U. V. Waghmare, N. A. Spaldin, K. M. Rabe, M. Wuttig and R. Ramesh: Epitaxial BiFeO₃ multiferroic thin film heterostructures. *Science* **299**, 1719 (2003).
7. T. Kimura, T. Goto, H. Shintani, K. Ishizaka, T. Arima and Y. Tokura: Magnetic control of ferroelectric polarization, *Nature* **426**, 55 (2003)
8. E. Ascher, H. Rieder, H. Schmid and H. Stössel: Some properties of ferromagnetoelectric nickel-iodine boracite, Ni₃B₇O₁₃I, *Journal of Applied Physics* **37**, 1404 (1966).
9. J. R. Teague, R. Gerson, and W. J. James: Dielectric hysteresis in single crystal BiFeO₃, *Solid State Communications* **8**, 1073 (1970).
10. S. V. Kiselev, R. P. Ozerov, and G. S. Zhdanov: Detection of magnetic order in ferroelectric BiFeO₃ by neutron diffraction, *Soviet Physics Doklady* **7**, 742 (1963).
11. J. F. Scott: Applications of magnetoelectrics, *Journal of Materials Chemistry* **22**,

- 4567 (2012).
12. F. Sugawara, S. Iida, Y. Syono, and S. Akimoto: Magnetic Properties and Crystal Distortions of BiMnO_3 and BiCrO_3 , *Journal of the Physical Society of Japan* **25**, 1553 (1968).
 13. G. A. Smolenskii and V. A. Bokov: Coexistence of magnetic and electric ordering in crystals, *Journal of Applied Physics* **35**, 915 (1964).
 14. N.A. Hill: Why are there so few magnetic ferroelectrics?, *The Journal of Physical Chemistry B* **104**, 6694 (2000).
 15. D.I. Khomskii: Multiferroics: Different ways to combine magnetism and ferroelectricity, *Journal of Magnetism and Magnetic Materials* **306**, 1 (2006).
 16. https://www.helmholtz-berlin.de/people/dimitri-argyriou/publications/archive_de.html
 17. I. A. Sergienko and E. Dagotto: Role of the Dzyaloshinskii-Moriya interaction in multiferroic perovskites, *Physical Review B* **73**, 094434 (2006).
 18. G. Lawes and G. Srinivasan: Introduction to magnetoelectric coupling and multiferroic films, *Journal of Physics D: Applied Physics* **44**, 243001 (2011).
 19. C.-W. Nan, M. I. Bichurin, S. Dong, D. Viehland, and G. Srinivasan: Multiferroic magnetoelectric composites: Historical perspective, status, and future directions, *Journal of Applied Physics* **103**, 031101 (2008).
 20. R. Waser, U. Böttger, and S. Tiedke, *Polar Oxides*, John Wiley & Sons, 2006
 21. G. Srinivasan, E. T. Rasmussen, J. Gallegos, R. Srinivasan, Y. I. Bokhan, V. M. Laletin: Magnetoelectric bilayer and multilayer structures of magnetostrictive and piezoelectric oxides, *Physical Review B* **64**, 214408 (2001).
 22. G. Srinivasan, E. T. Rasmussen, B. J. Levin, R. Hayes: Magnetoelectric effects in bilayers and multilayers of magnetostrictive and piezoelectric perovskite oxides, *Physical Review B* **65**, 134402 (2002).

23. H. Zheng, J. Wang, S. E. Lofland, Z. Ma, L. Mohaddes-Ardabili, T. Zhao, L. Salamanca-Riba, S. R. Shinde, S. B. Ogale, F. Bai, D. Viehland, Y. Jia, D. G. Schlom, M. Wuttig, A. Roytburd, R. Ramesh: Multiferroic BaTiO₃- CoFe₂O₄ nanostructures, *Science* **303**, 661 (2004).
24. J. G. Brookshear, *Computer Science: An Overview*, Addison Wesley 2011
25. J. Brewer and M. Gill, *Nonvolatile Memory Technologies with Emphasis on Flash: A Comprehensive Guide to Understanding and Using Flash Memory Devices*, John Wiley & Sons 2011.
26. C. Chappert, A. Fert and F. N. Van Dau, The emergence of spin electronics in data storage, *Nature materials* **6**, 813 (2007)
27. Y.-H. Chu, L. W. Martin, M. B. Holcomb, M. Gajek, S.-J. Han, Q. He, N. Balke, C.-H. Yang, D. Lee, W. Hu, Q. Zhan, P.-L. Yang, A. Fraile-Rodriguez, A. Scholl, S. X. Wang, and R. Ramesh: Electric-field control of local ferromagnetism using a magnetoelectric multiferroic, *Nature Materials* **7**, 478 (2008).
28. J.F. Scott: Data storage Multiferroic memories, *Nature materials* **6**, 256 (2007)
29. M. Gajek, M. Bibes, S. Fusil, K. Bouzehouane, J. Fontcuberta, A. Barthelemy, A. Fert: Tunnel junctions with multiferroic barriers, *Nature materials* **6**, 296 (2007)
30. S. Dong, J. Zhai, F. Bai, J.-F. Li, D. Viehland: Push-pull mode magnetostrictive/piezoelectric laminate composite with an enhanced magnetoelectric voltage coefficient, *Applied Physics Letters* **87**, 062502 (2005)
31. F. Sugawara and S. Iida: New Magnetic Perovskite of BiMnO₃ and BiCrO₃, *Journal of the Physical Society of Japan* **20**, 1529 (1965).
32. T. Atou, H. Chiba, K. Ohoyama, Y. Yamaguichi, Y. Syono: Structure determination of ferromagnetic perovskite BiMnO₃, *Journal of Solid State Chemistry* **145**:639 (1999).
33. A. A. Belik, S. Iikubo, T. Yokosawa, K. Kodama, N. Igawa, S. Shamoto, M.

- Azuma, M. Takano, K. Kimoto, Y. Matsui, E. Takayama-Muromachi: Origin of the Monoclinic-to-Monoclinic Phase Transition and Evidence for the Centrosymmetric Crystal Structure of BiMnO₃, *Journal of the American Chemical Society* **129**, 971 (2007).
34. T. Kimura, S. Kawamoto, I. Yamada, M. Azuma, M. Takano, and Y. Tokura: Magnetocapacitance effect in multiferroic BiMnO₃, *Physical Review B* **67**, 180401 (2003).
 35. E. Montanari, G. Calestani, A. Migliori, M. Dapiaggi, F. Bolzoni, R. Cabassi, and E. Gilioli: High-temperature polymorphism in metastable BiMnO₃, *Chemistry of Materials* **17**, 6457 (2005).
 36. A. A. Belik: Polar and nonpolar phases of BiMO₃: A review, *Journal of Solid State Chemistry* **195**, 32 (2012).
 37. E. M. Levin, C. R. Robbins, and H. F. McMurdie (eds), Phase Diagrams for Ceramists, Vol. 1, p. 127. American Ceramic Society, Columbus, 1964
 38. A.F. Moreira dos Santos, A.K. Cheetham, W. Tian, X. Pan, Y. Jia, N.J. Murphy, J. Lettieri, D.G. Schlom: Epitaxial growth and properties of metastable BiMnO₃ thin films, *Applied physics Letters* **84**, 91 (2004).
 39. W. Eerenstein, F. D. Morrison, J. F. Scott, N. D. Mathur: Growth of highly resistive BiMnO₃ films, *Applied Physics Letters* **87**, 101906 (2005).
 40. M. Gajek, M. Bibes, A. Barthélémy, K. Bouzehouane, S. Fusil, M. Varela, J. Fontcuberta, and A. Fert: Spin filtering through ferromagnetic BiMnO₃ tunnel barriers, *Physical Review B* **72**, 020406 (2005).
 41. S. J. Blundell, *Magnetism in condensed matter*, Oxford University Press 2001
 42. E. Montanari, G. Calestani, L. Righi, E. Gilioli, F. Bolzoni, K.S. Knight, and P.G. Radaelli: Structural anomalies at the magnetic transition in centrosymmetric BiMnO₃, *Physical Review B* **75**, 220101 (2007).

43. W.-T. Chen, F. Sher, N. D. Mathur, C. M. Kavanagh, F. D. Morrison, and J. P. Attfield: Structural, Magnetic, and Electrical Properties of $\text{Bi}_{1-x}\text{La}_x\text{MnO}_3$ ($x = 0.0, 0.1, \text{ and } 0.2$) Solid Solutions, *Chemistry of Materials* **24**, 199 (2012).
44. A. Moreira dos Santos, A. K. Cheetham, T. Atou, Y. Syono, Y. Yamaguchi, K. Ohoyama, and H. Chiba: Orbital ordering as the determinant for ferromagnetism in biferroic BiMnO_3 , *Physical Review B* **66**, 064425 (2002).
45. I.V. Solovyev and Z.V. Pchelkina: Orbital ordering and magnetic interactions in BiMnO_3 , *New Journal of Physics* **10**, 073021 (2008).
46. A. Moreira dos Santos, S. Parashar, A. R. Raju, Y. S. Zhao, A. K. Cheetham, C. N. R. Rao: Evidence for the likely occurrence of magnetoferroelectricity in the simple perovskite, BiMnO_3 , *Solid State communications* **122**, 49 (2002).
47. Z. H. Chi, H. Yang, S. M. Feng, F. Y. Li, R. C. Yu, C. Q. Jin: Room-temperature ferroelectric polarization in multiferroic BiMnO_3 , *Journal of Magnetism and Magnetic Materials* **310**, e358 (2007).
48. J.Y. Son and Y.-H. Shin: Multiferroic BiMnO_3 thin films with double SrTiO_3 buffer layers, *Applied Physics Letters* **93**, 062902 (2008).
49. H. Jeon, G. Singh-Bhalla, P. R. Mickel, K. Voigt, C. Morien, S. Tongay, A. F. Hebard, and A. Biswas: Growth and characterization of multiferroic BiMnO_3 thin films, *Journal of Applied Physics* **109**, 074104 (2011).
50. P. Baettig, R. Seshadri, N.A. Spaldin: Anti-polarity in ideal BiMnO_3 , *Journal of the American Chemical Society* **129**, 9854 (2007).
51. I.V. Solovyev and Z.V. Pchelkina: Magnetic ground state and multiferroicity in BiMnO_3 , *JETP letters* **89**, 597 (2009).
52. G. Catalan: Magnetocapacitance without magnetoelectric coupling, *Applied physics letters* **88**, 102902 (2006).
53. L. B. Freund and S. Suresh, *Thin Film Materials: Stress, Defect Formation and*

Surface Evolution, Cambridge University Press 2004.

54. O. Y. Gorbenko, S. V. Samoilenkov, I. E. Graboy, and A. R. Kaul: Epitaxial stabilization of oxides in thin films, *Chemistry of Materials* **10**, 4026 (2002).
55. J. Narayan and B.C. Larson: Domain epitaxy: A unified paradigm for thin film growth, *Journal of applied physics* **93**, 278 (2003).
56. T. Zheleva, K. Jagannadham, and J. Narayan: Epitaxial growth in large-lattice-mismatch systems, *Journal of Applied Physics* **75**, 860 (1994).
57. J. C. Miller, R. F. Haglund, *Laser Ablation and Desorption*, Academic Press 1998.
58. L.W. Martin, Y.-H. Chu, R Ramesh: Advances in the growth and characterization of magnetic, ferroelectric, and multiferroic oxide thin films, *Materials Science and Engineering: R: Reports* **68**, 89 (2010).
59. B. D. Cullity, *Elements of X Ray Diffraction*, BiblioBazaar 2011.
60. http://www.globe-expert.eu/quixplorer/filestorage/Interfocus/6-Science_Technologie/60-Generalites/60-SRCNL-AZoM_com_Engineering_and_Materials_Articles_Feed/200904/X-Ray_Powder_Diffraction_XRPD_-_Detection_of_Low_Amounts_of_Crystalline_Impurities_for_Pharmaceutical_Process_Control_by_PANalytical....html
61. Speller, S. Texture XRD. [cited 2011 12/01/2011]; Available from: <http://weblearn.ox.ac.uk/site/users/trin0342/training/texture/>.
62. S. J. B. Reed, *Electron Microprobe Analysis and Scanning Electron Microscopy in Geology*, Cambridge University Press 2005.
63. Density Determination Kit User's Manual, Sartorius
64. Dektak 150 Surface Profiler User's Manual, Veeco Instruments Inc.
65. Physical Property Measurement System Vibrating Sample Magnetometer (VSM) Option User's Manual, Quantum Design,

66. Y. Liu, D. J. Sellmyer and D. Shindo, *Handbook of Advanced Magnetic Material*, Springer 2005.
67. Discussion with Dr. Peter K Petrov.
68. S. S. Zumdahl, *Chemical Principles*, Cengage Learning 2009.
69. J. A. Dean, *Lange's handbook of chemistry*, McGraw-Hill 1999.

Appendices

Appendix A Estimation of Errors

When we measure a physical quantity, we do not expect the value obtained to be exactly equal to the true value. It is important to give some indication of how close the result is likely to be to the true value. An estimate of the error in the result is necessary, because without them we cannot draw significant conclusions from the experimental results. Errors may be divided into two kinds, systematic and random. A systematic error is one which is constant throughout a set of readings. A common source of systematic error is inaccurate apparatus. A random error is one which varies and which is equally likely to be positive or negative. They cause successive readings to spread about the true value of the quantity.

Suppose we make a set of measurements of the same quantity. We assume throughout that no systematic errors are present. The individual values x_1, x_2 , etc., vary owing to random errors, and the mean value \bar{x} (i.e. the arithmetic average) is taken as the best value of the quantity. The most we can do is to say that there is a certain probability that X lies within a certain range centred on \bar{x} . the probability tends to a Gaussian distribution. The results of the measurements are quoted as " $\bar{x} \pm \sigma_m$ ", and σ_m is standard deviation of this distribution. σ_m can be calculated by the following equations.

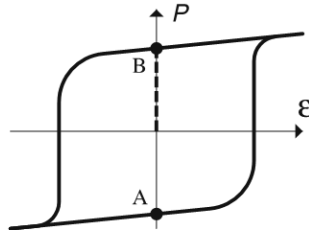
$$s^2 = \frac{1}{n} \sum d_i^2$$
$$\sigma \approx \left[\frac{n}{n-1} \right]^{\frac{1}{2}} s$$
$$\sigma_m = \frac{\sigma}{\sqrt{n}}$$

Appendix B Ferroelectric Measurement

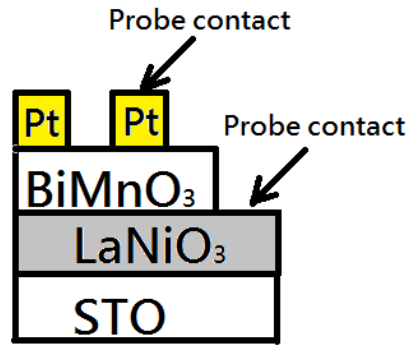
The electrical properties of a ferroelectric film can only be measured when it is fabricated as a device (most typically a capacitor). When a voltage is applied across a capacitor, one electrode becomes positively charged, the other negatively charged, with the corresponding electric field directed from the positive to the negative. A charge of $+Q$ is stored on the top electrode and $-Q$ on the bottom one. Electrons are caused to flow from the positive to the negative plate by the external voltage. The experimental setup typically measures the integrated macroscopic current flowing through the sample, as in (11).

$$\Delta P = P(\Delta t) - P(0) = \int_0^{\Delta t} dt j(t)$$

The observation of an electric hysteresis loop (Fig. 1) is considered necessary to establish ferroelectricity. The difference of $P_B - P_A$ defines the magnitude P_s of the spontaneous polarization in the vertical direction.



To perform ferroelectric measurement on BiMnO_3 , it is necessary to fabricate a layered device whose structure is $\text{SrTiO}_3/\text{LaNiO}_3/\text{BiMnO}_3/\text{Pt}$, as shown in Figure 1.7. SrTiO_3 serves as a substrate, and LaNiO_3 is used as the bottom electrode material. Pt serves as the top electrode.



Many conductive oxides and substrates have been discovered, but LaNiO₃ was selected as the bottom electrode material for four reasons. First, LaNiO₃ exhibits a good metallic behavior with a resistivity of $10^{-5} \Omega\text{m}$ at 300K. Second, unlike ferromagnetic and metallic SrRuO₃, LaNiO₃ is paramagnetic over the temperature range of 300K to 1.5K, thus lowering the magnetic effect on BiMnO₃ during measurements. Third, LaNiO₃ has a pseudocubic perovskite structure with the lattice constant of 3.84Å, similar to the lattice constant of SrTiO₃. This is favorable for epitaxial growth. Fourth, there is a cost advantage in comparison with metallic Nb-doped SrTiO₃ substrates. LaNiO₃ thin films have been demonstrated to be epitaxially grown on the SrTiO₃ substrate. LaNiO₃ bulk materials can be prepared using several methods such as sol-gel processing, powder coprecipitation and nitrate decomposition. The film of LaNiO₃ has been grown using r-f sputtering, pulsed laser deposition, chemical solution deposition.

The fabrication of the top electrode involves the lift-off technique in semiconductor lithography. The sample with BiMnO₃ is first spin-coated with a thin layer of photoresist, and then the photoresist is soft baked for further drying and strengthening the adhesion. The photoresist is patterned by being exposed to light via a pattern-carrying mask. The exposed area is removed in a solvent called developer

since the exposed areas of the photoresist exhibit a greater solubility in a developer than the non-exposed areas. A thin layer of either gold or platinum is then deposited on the remaining photoresist and the exposed BiMnO₃ thin film. Using an appropriate solvent, the remaining parts of the photoresist and the deposited metal film atop these parts of the photoresist are lifted off, leaving the gold or platinum electrode on selective areas of BiMnO₃ to form a device for ferroelectric measurements.

Appendix C User's Manual for Pulsed Laser Deposition (PLD)

Entering the PLD Lab

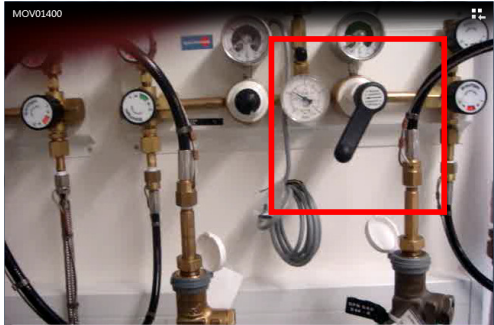
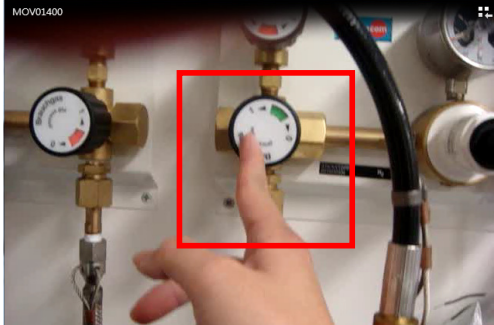




One must close the outermost door behind them to prevent unauthorized access. First user of the day must switch on the lights to the PLD lab. Check that the ventilation system is working and there is no gas alarm. Wear Lab coat, overshoes, gloves, and protective goggles. Check whether the red warning lamp (“laser on”) is flashing. If the red lamp is “on”, authorized people are required to wear goggles before entering the PLD room.

If you are the first person to enter the lab, you should switch on the laser, but if you are not, someone might switch it on already. Make sure that the laser shutter closes the laser output window off! There are two switch buttons, one is bigger and red; another one is with a key. When you are going to switch on the laser, you should switch the red one first and wait for about 2 min and turn another one.

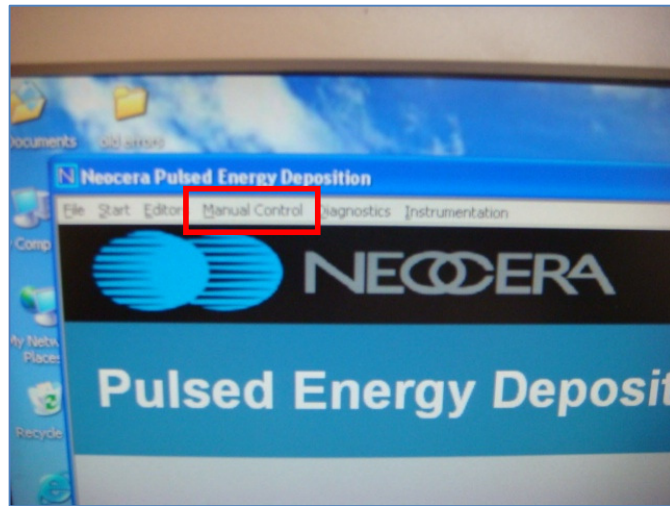
First of all, clean the substrates with acetone in ultrasonic bath for 3 minutes, and then repeat in order the same cleaning processes in isopropanol and distill water. Blow and dry the substrates using a nitrogen air gun.

	
<p>Clean the beaker using distilled water</p>	<p>Put the substrate in the beaker with acetone</p>
	
<p>Put the beaker in ultrasonic bath</p>	<p>Set cleaning time to be 3 min</p>
	
<p>Clean for 3 min.</p>	

Ensure that the oxygen and nitrogen gas cylinders are open with enough volume of gas

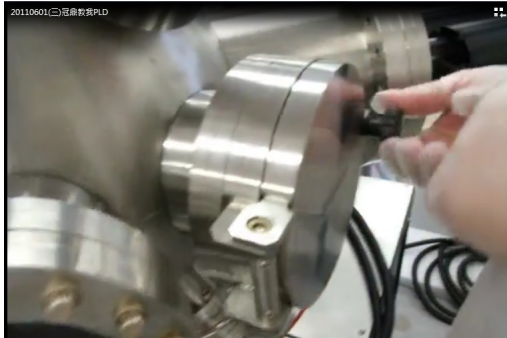
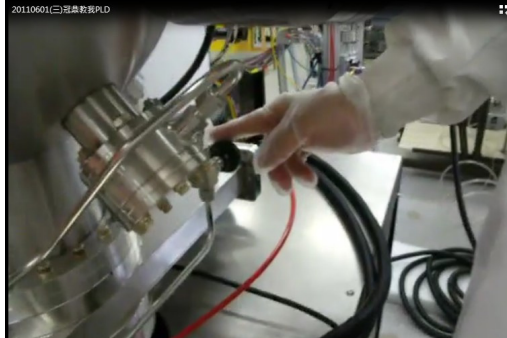
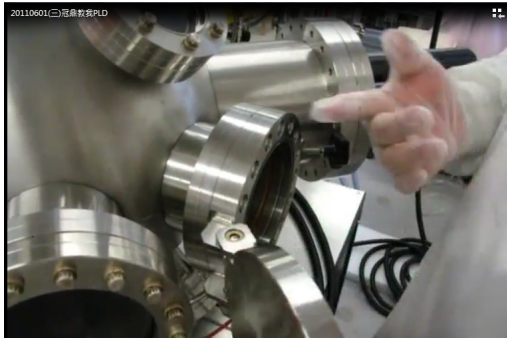
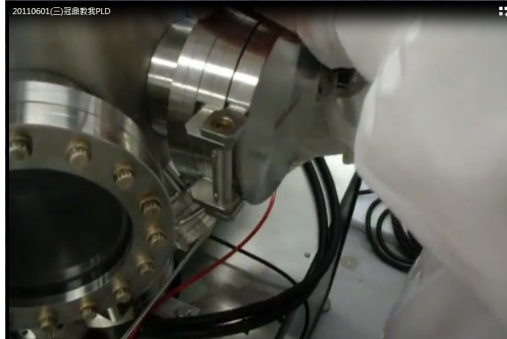




		
<p>The handle indicates an arrow representing to the valve which should be opened and the cylinder which is using</p>	<p>Make sure the switch is on with green color</p>	
		
<p>Make sure black pointer above red pointer in the flow meter</p>		
		
<p>Make sure the direction of handle is toward O2 cylinder.</p>	<p>Make sure the switch is on with green color</p>	<p>Make sure black pointer above red pointer in the flow meter</p>


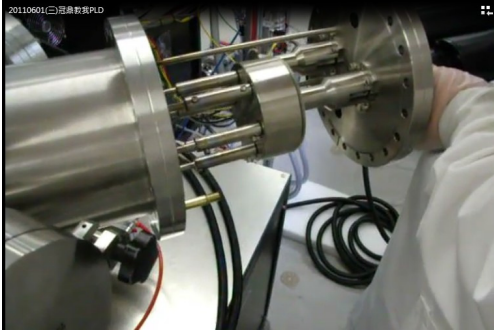





Ensure that the computer corresponding for that chamber is running. Open PLD Neocera software. Open the 'Advanced Vacuum Control' from the 'Manual Control' tool bar









Press the icon called Pulsed Laser Deposition. The PLD system have three main panels. The first step is to make sure "gate valve" is closed.

<p>Feedback</p> <p>Turbo pump status <input type="text"/></p> <p>Actual Rotation Speed <input type="text"/></p> <p>Set Rotation Speed <input type="text"/></p> <p>Ch. High Pressure <input type="text"/> <input type="text"/> Set speed</p> <p>Ch. Low Pressure <input type="text"/></p> <p>Vacuum Control Status <input type="text"/></p>	<p>Valve control</p> <p>Gate Valve Status <input type="text" value="close"/></p>	<p><input type="button" value="Close gate valve"/></p> <p><input type="button" value="Open gate valve"/></p> <p><input type="button" value="Open Rough valve"/></p> <p><input type="button" value="Open Rough valve"/></p>						
	<p>Chamber pump down</p> <table border="1"> <tr> <td><input type="button" value="Shutdown Turbo With Vent"/></td> <td><input type="button" value="Rough pump on"/></td> <td><input type="button" value="Start pumpdown"/></td> </tr> <tr> <td><input type="button" value="Shutdown Turbo Without Vent"/></td> <td><input type="button" value="Rough pump off"/></td> <td><input type="button" value="Abort pumpdown"/></td> </tr> </table> <p>Pumpdown Status <input type="text" value="close"/></p>	<input type="button" value="Shutdown Turbo With Vent"/>	<input type="button" value="Rough pump on"/>	<input type="button" value="Start pumpdown"/>	<input type="button" value="Shutdown Turbo Without Vent"/>	<input type="button" value="Rough pump off"/>	<input type="button" value="Abort pumpdown"/>	<p>Chamber purge/backfill</p> <p>MFC Number <input type="text" value="close"/></p> <p>Backfill Setpoint <input type="text" value="close"/></p> <p>Backfill Status <input type="text" value="close"/></p> <p><input type="button" value="Initiate Camber Purge/ Backfill"/></p> <p><input type="button" value="Abort Purge"/></p>
<input type="button" value="Shutdown Turbo With Vent"/>	<input type="button" value="Rough pump on"/>	<input type="button" value="Start pumpdown"/>						
<input type="button" value="Shutdown Turbo Without Vent"/>	<input type="button" value="Rough pump off"/>	<input type="button" value="Abort pumpdown"/>						

	
<p>loosen the screw of the main chamber door.</p>	<p>Vent the chamber by turning the knob below the chamber</p>
	
<p>the main chamber door can open after breaking the vacuum.</p>	<p>tighten the knob</p>
	
<p>tighten the screw for the chamber door.</p>	<p>Put the foam stage on the working table.</p>
	
<p>loosen the screws of the target motor.</p>	<p>Hand the heavy target motor very</p>

	<p>carefully. Please don't touch the wire connection, please be careful.</p> 
	
<p>begin to slowly it out.</p>	<p>Put the target motor upright on the foam stage.</p>
	
<p>Loosen the bolts on the target shutter</p>	<p>Loosen the bolts on the target shutter</p>
	
	<p>Clean the target shutter surface with</p>

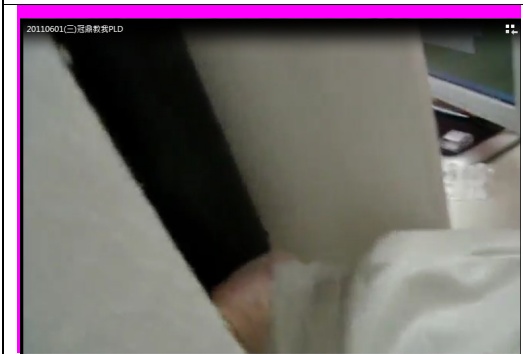
	<p>isopropanol and tissue</p> 
<p>Clean the target shutter surface with isopropanol and tissue</p>	
	
<p>The home position of target is set to be 180 degree.</p>	<p>Loose the screws in the target holder.</p>
	
<p>Place the target holder back on the rod and ensure that its height is just below the circular opening then screw the holder in position (128mm in height so the substrate-target distance is maintained at 50mm)</p>	<p>Now the target on the holder is mounted.</p>



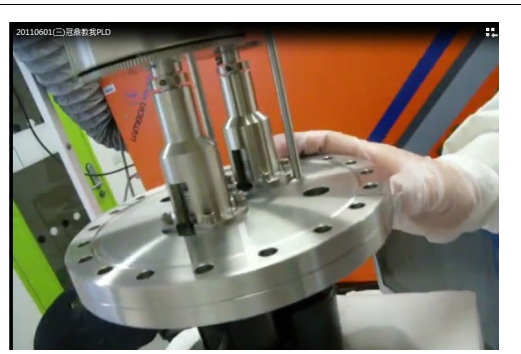
Mount the shutter back to its original position.



Clean using compressed air.



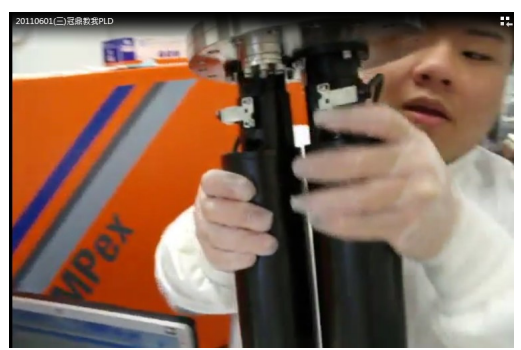
Lift the Motor unit from the black cylinders by one hand.



Lift the target motor up by one hand from the bottom of the motor and hold on the side by another hand.



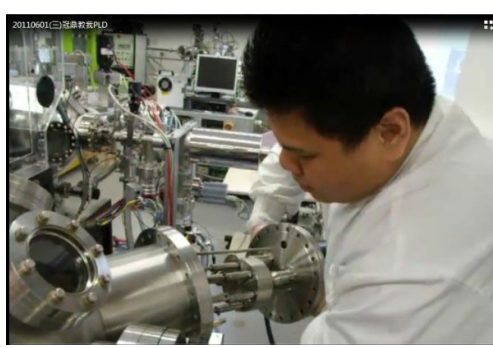
Be careful It is very heavy.



Place each hand on the black cylindrical structure



Remember don't break the wire!!!



Place the target motor unit back into the chamber



Ensure that the scribed arrow on the stainless steel rim is on top and at right position.



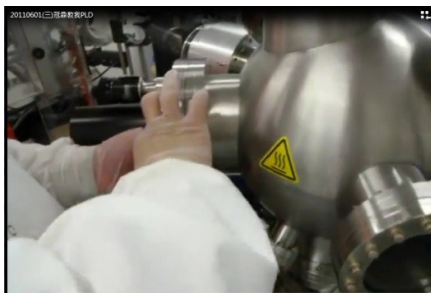
Re-connect the X and Y cables and also make sure they are at right positions



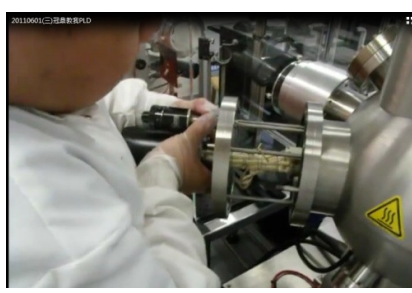
Re-connect the X and Y cables



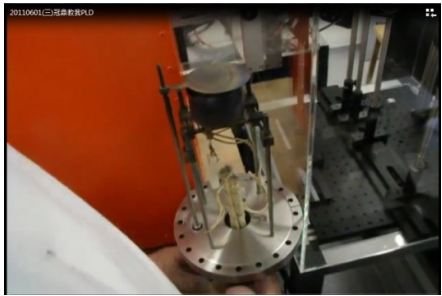
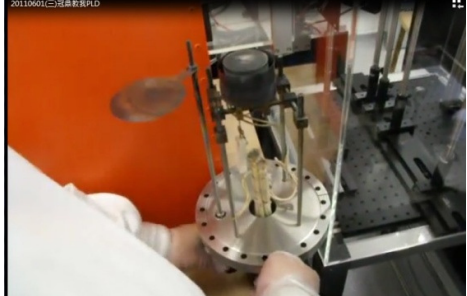


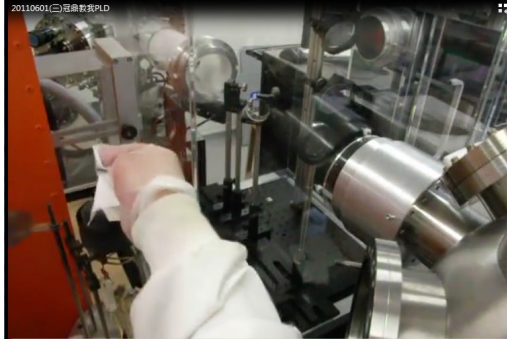
Tighten the screw of the chamber door



loosen the screw of the chamber door.



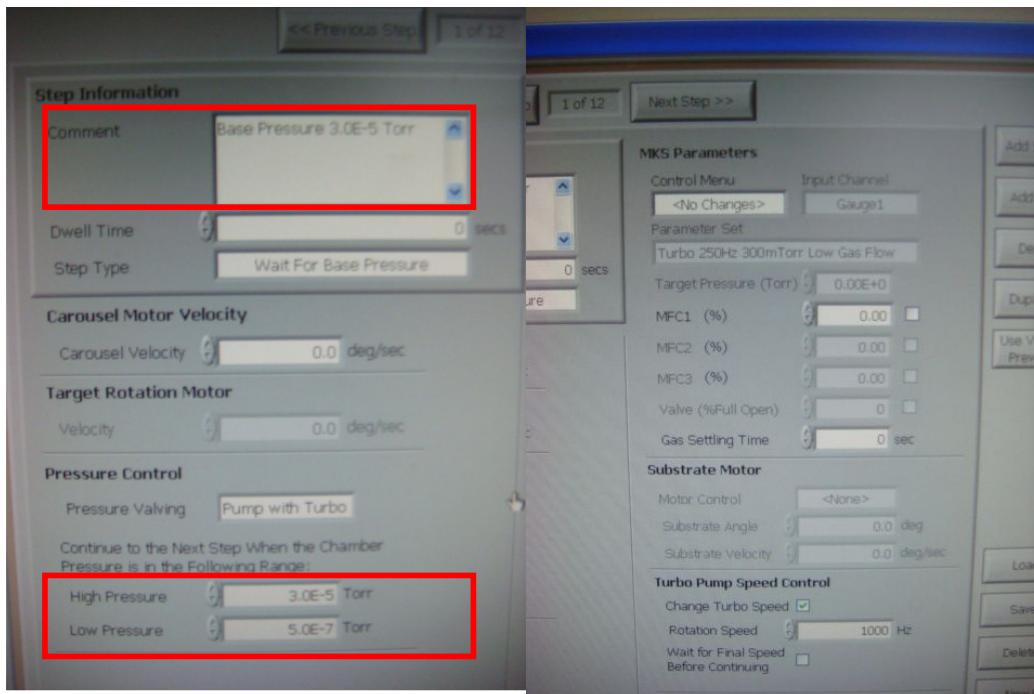
begin to slowly it out.

	
<p>Put the substrate holder on the table.</p>	<p>Open the shutter</p>
	
<p>Clean the holder surface with SiC paper and isopropanol in order to remove the silver paint</p>	
	
<p>Clean the surface with isopropanol and tissues.</p>	<p>spread some silver glue in the centre of the stainless steel substrate holder</p>
<p>Place the substrate on the glue (good side up), wrap some tissue around the tweezers and carefully press the substrate down</p>	<p>Heat substrate holder to 40°C at the ramp rate (1°C/min) using Heater Control panel</p>
<p>Heat substrate holder to 80°C at the ramp rate (5°C/min) using Heater Control panel</p>	<p>After reaching 80°C, place the substrate holder back into the chamber</p>

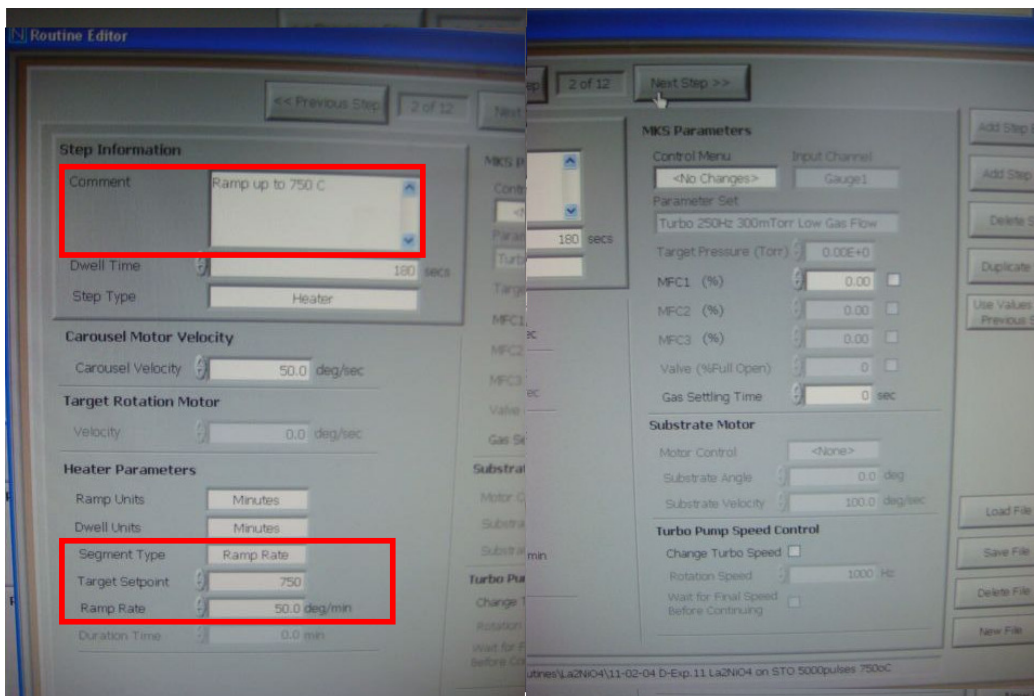
Heater Control	
System Heater	
Heater to Control	
Heater Feedback	
Temperature	
Target Setpoint	
Heater Control	
Control Type	<input type="text" value="Ramp Rate"/>
Setpoint	<input type="text" value="40"/>
Ramp time	
Ramp rate	<input type="text" value="1.0"/>
Status	
Automatic Reset/Shut-off	
Reset After	
Time Remaining	
Pleiffer	
Heater Status	
Heater	

- press → set up the routine (routine editor, load the file, choose your routine)(Fig3)

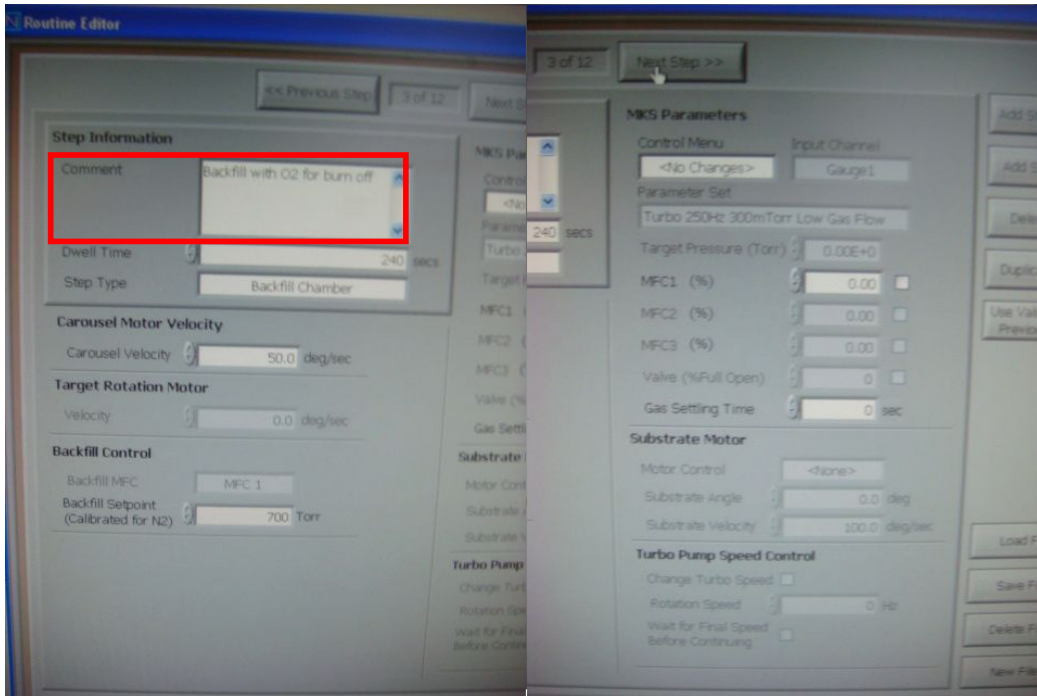
Step1 (Comment: Base Pressure 3.0E-5 Torr, High Pressure: 3.0E-5 Torr, Low Pressure: 5.0E-7 Torr)



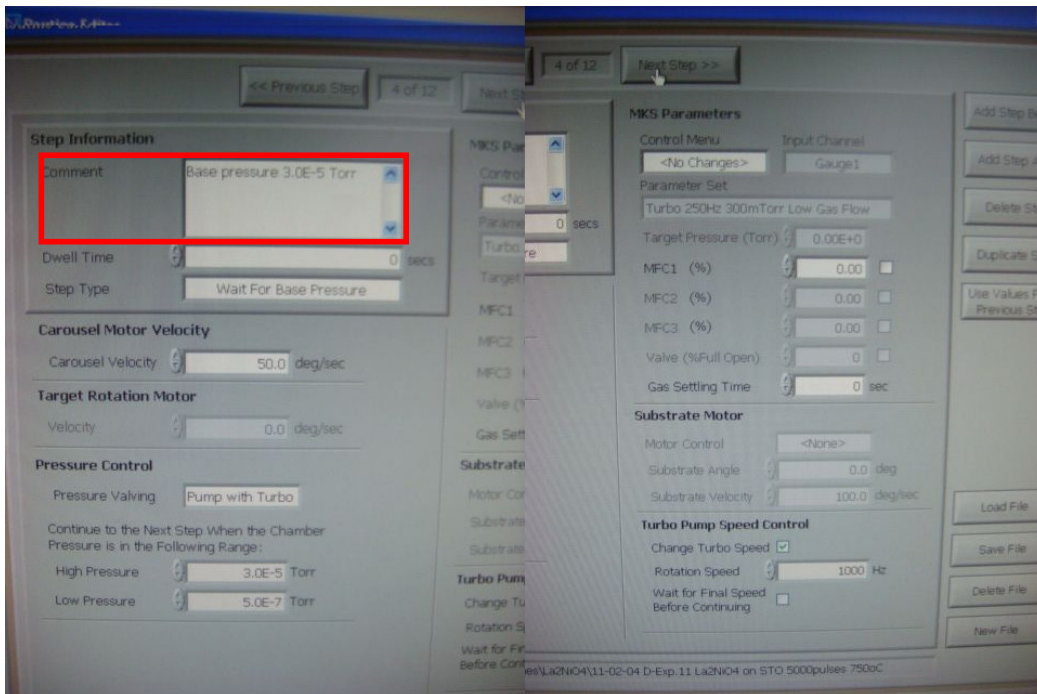
Step2 (Comment: Ramp up to 700°C, Target setpoint: 700, Ramp Rate: 50°C/min)



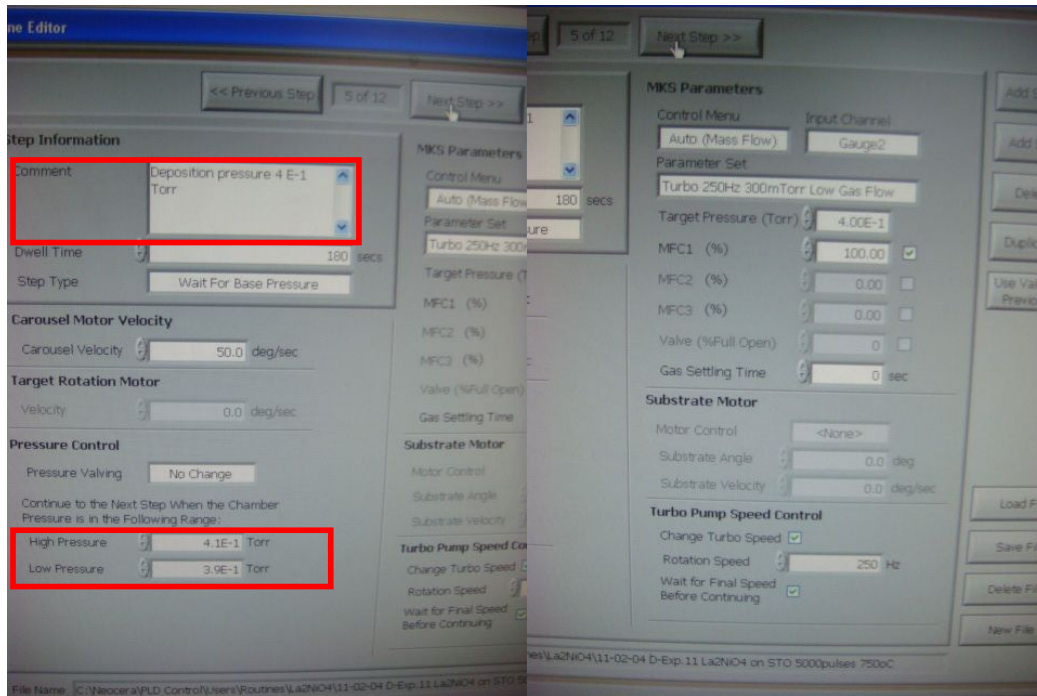
Step3 (Comment: Backfill with O2 for burn off)



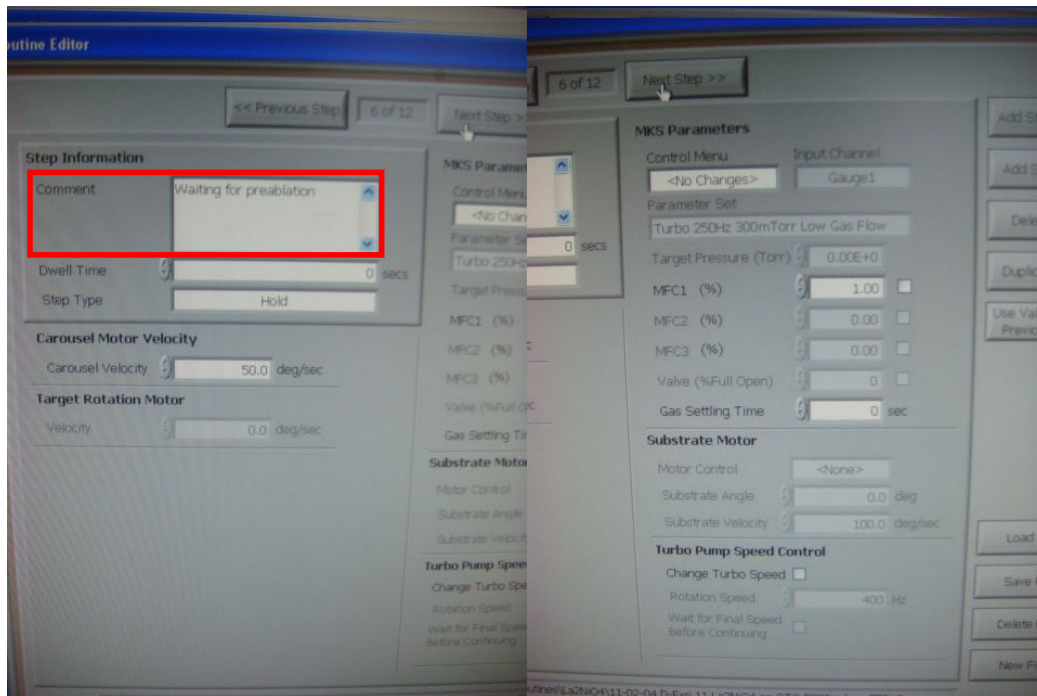
Step4 (Comment: Base pressure 3.0E-5 Torr)



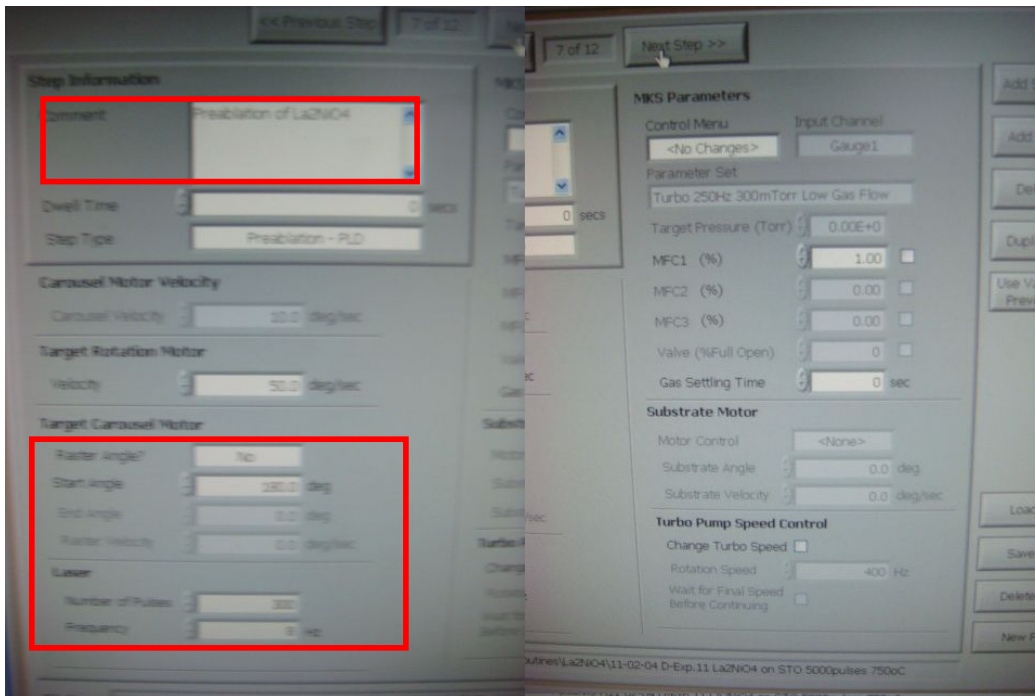
Step5 (Comment: Deposition pressure 1.5E-1 Torr, High Pressure: , Low Pressure:)
Down to the working pressure which is set by the routine.



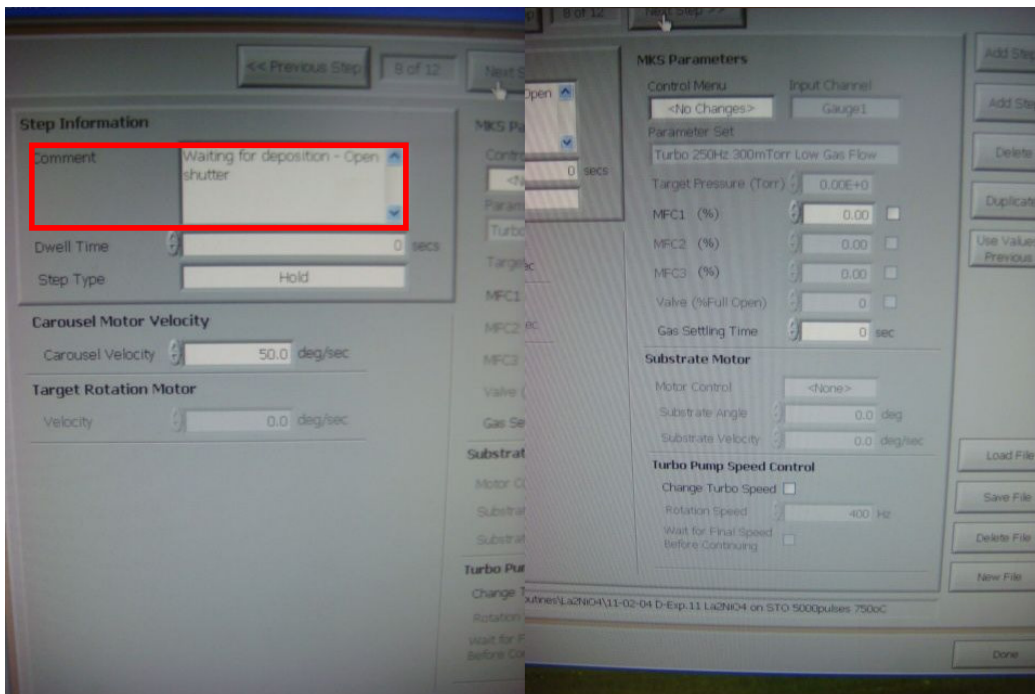
Step6 (Comment: Waiting for pre-ablation)



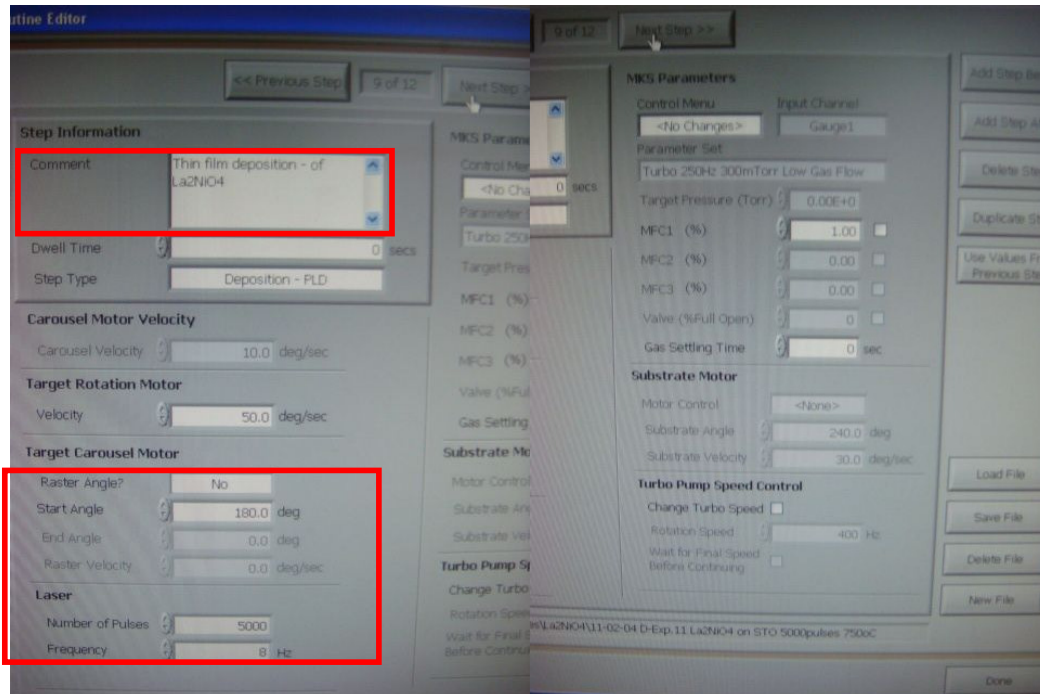
Step7 (Comment: pre-ablation, start angle is set to be 180, the number of pulse is set at 300)



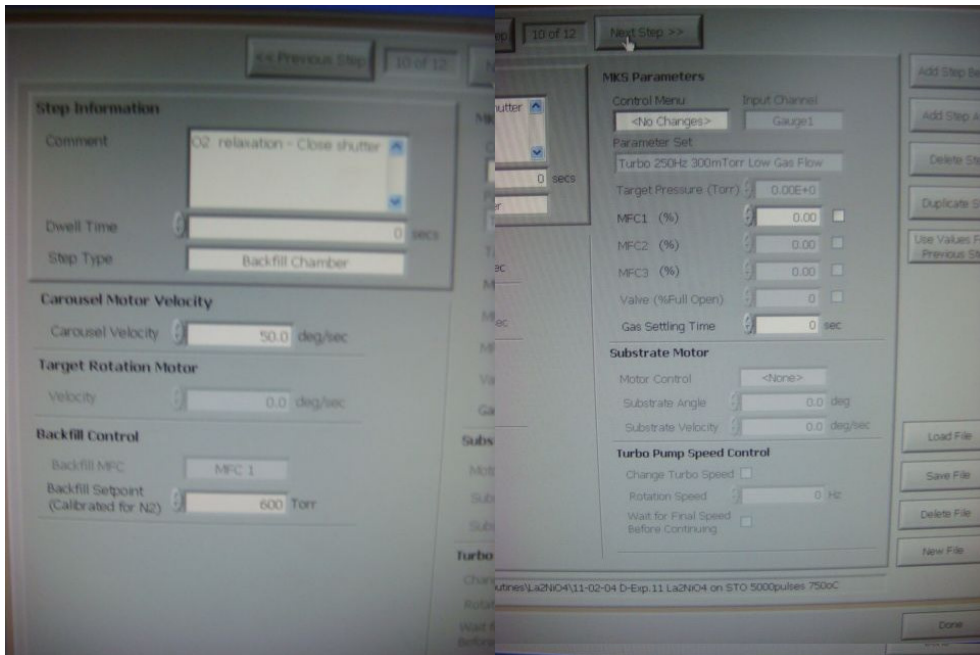
Step8 (Comment: Waiting for deposition)



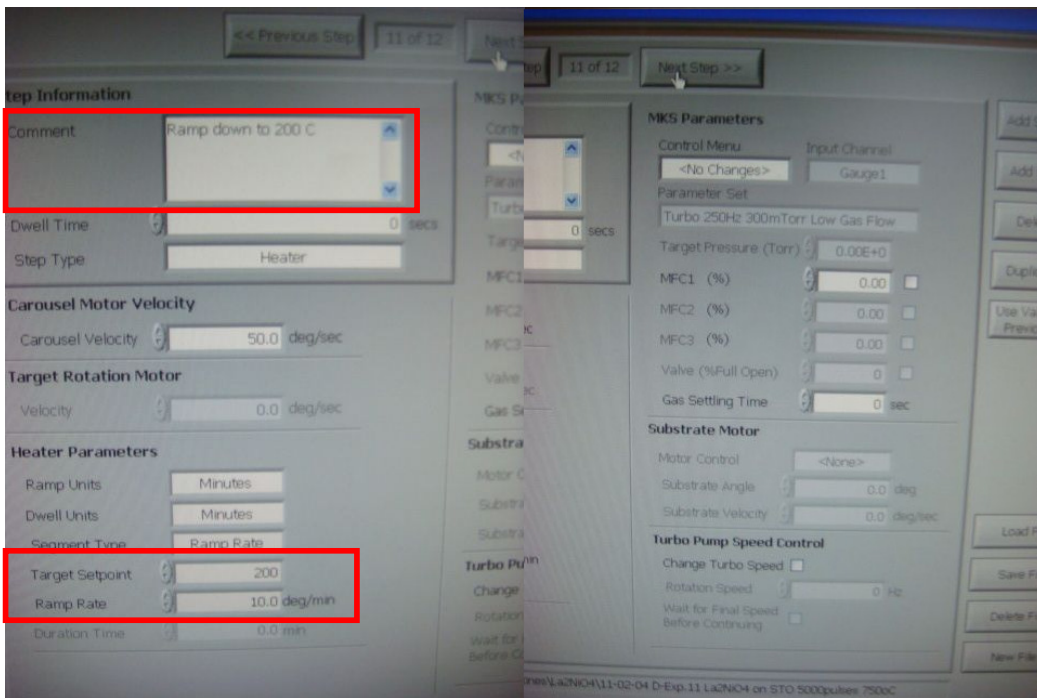
Step9 (Comment: Thin film deposition, start angle is set to be 180, the number of pulse is set to be 3000 at first time because this value might achieve 100 nm based on Kuan-Ting's experience. Different materials can make different growing rate. This parameter requires further confirmation by further trials.)



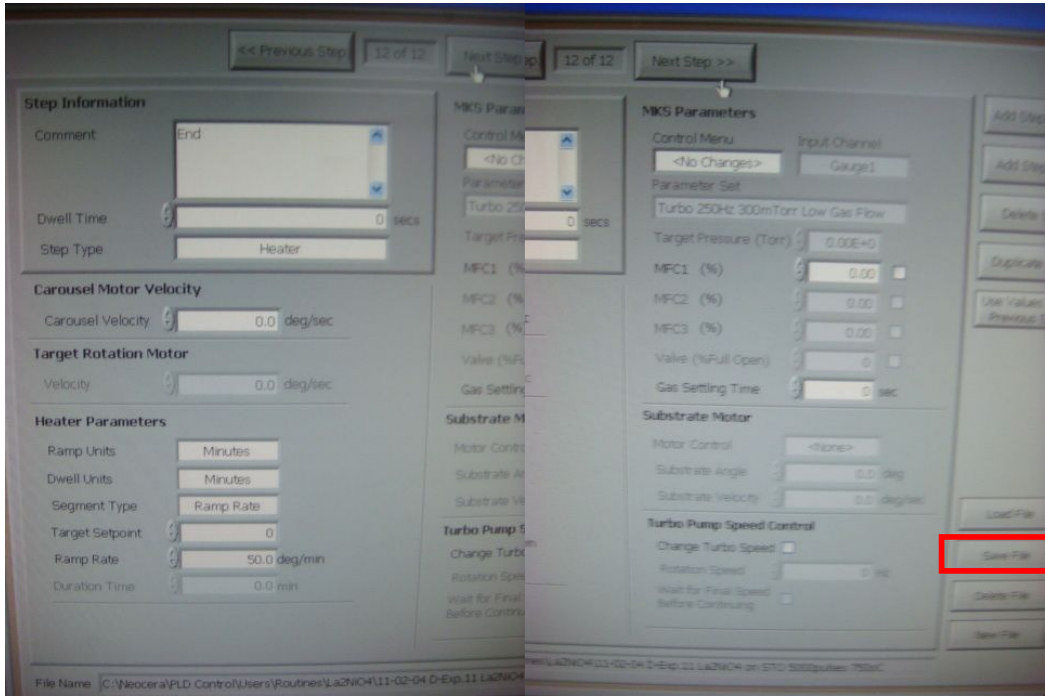
Step10 (Comment: O₂ Backfill chamber relaxation-close shutter, I don't need to change it)



Step11 (Comment: Ramp down to 200°C, 10°C/min)



Step12 (Comment: End)

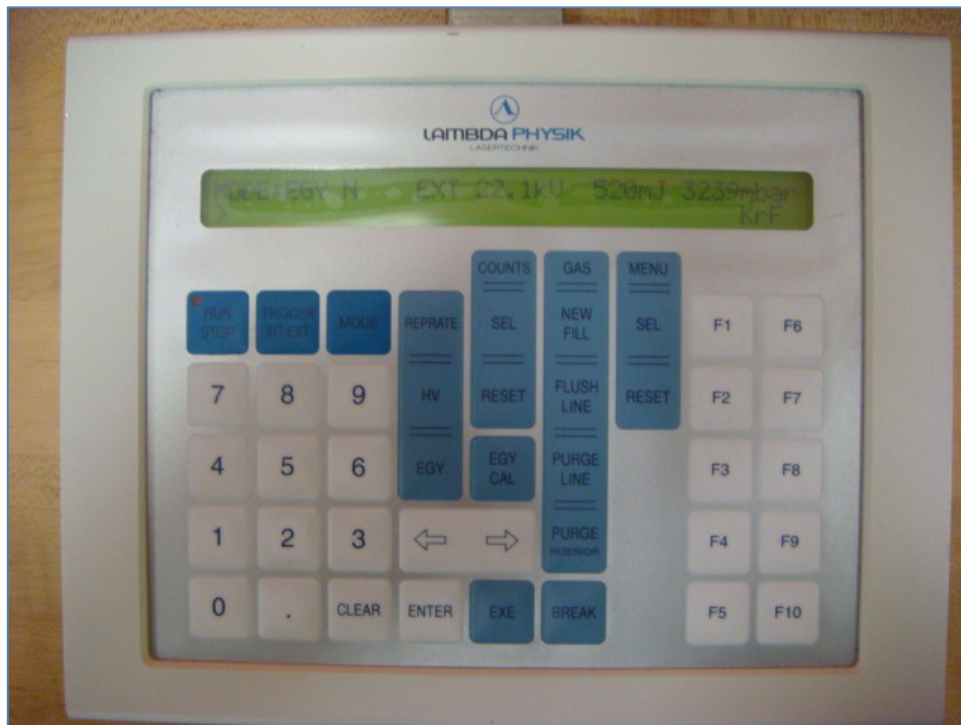


- Load and set routine
- Press “Save File” → Press “Done”

- Before press “start routine“, make sure that both “Home Carousel Motor” and “Enable Target DC Rotation Motor” are green on, and then Load the routine we saved before, and press “start routine” in PED panel.

PED/PLD Control Panel											
Target Motors Feedback Target Motor position <input type="text"/> Target Motor velocity <input type="text"/> Target DC motor Velocity <input type="text"/>		Substrate Heater Feedback Temperature <input type="text"/> Target Setpoint <input type="text"/>									
Substrate Motor Feedback Substrate Motor Position <input type="text"/> Substrate Motor Velocity <input type="text"/>		Laser Feedback Shots Remaining <input type="text"/> Turbo pump Rotation Speed									
Beam Scan Motor Feedback Beam Scan Position <input type="text"/> Beam Scan Velocity <input type="text"/>		Substrate Z motor Substrate Z position Heater Z motor Heater Z position									
PLD Routine Information Current Step Number <input type="text"/> Step Comment <input type="text"/> PLD Execution Status <input type="text"/>											
PLD Routine Control <div style="display: flex; align-items: center; margin-bottom: 10px;"> <div style="border: 1px solid black; padding: 5px; margin-right: 10px;">Load Routine</div> <input style="width: 300px;" type="text"/> </div> <table border="1" style="width: 100%; text-align: center; border-collapse: collapse;"> <tr> <td style="width: 25%;">Start Routine</td> <td style="width: 25%;">Hold Routine</td> <td style="width: 25%;">Resume Routine</td> <td style="width: 25%;">Abort Routine/ Homing</td> </tr> <tr> <td>Home Carousel Motor</td> <td>Enable Target DC Rotation Motor</td> <td>Home Substrate Motor</td> <td></td> </tr> </table>				Start Routine	Hold Routine	Resume Routine	Abort Routine/ Homing	Home Carousel Motor	Enable Target DC Rotation Motor	Home Substrate Motor	
Start Routine	Hold Routine	Resume Routine	Abort Routine/ Homing								
Home Carousel Motor	Enable Target DC Rotation Motor	Home Substrate Motor									
PED Status HV PS status <input type="radio"/> HV standby PED interface <input type="radio"/> Fnng <input type="radio"/> PED status Pulse Count Voltage Remaining time											
PED system Configuration Source 1 installed Source 1 installed											
PED Interlocks											

- **Preparation for Pre-ablation (Step6)**
- Ask everyone in the lab to put on the safety goggles! Lock the Lab door. Make sure that the mirror is located at 28.35 (Don't touch the mirror!). Check the laser control is set to external, press "run laser" and "EXE". Check the laser shutter is open. Ensure the substrate shutter is closed. When you are absolutely ready to proceed, click 'resume routine' in the 'PED/PLD control panel' window.



- After you are ready for running the laser, that is at Step 6, turn on laser by pressing 'RUN' followed by 'EXE' on laser control pad. Check laser control is set to external control by pressing 'Trigger Int/Ext' 'RUN' -> 'ENTER'. Normally set the voltage to 23~25 kV so that the laser is set at 520 mJ of power. Press 'HV', to change the value of voltage then press 'ENTER'. Don't press other functional buttons. If accidentally press "MODE" or "EGY" and enter them, please inform it to Dr Peter Petrov or Dr Bin Zou immediately.

- **Pre-ablation(Step7)**

- **Preparation for ablation (Step8)**

open the substrate shutter, but make sure it doesn't touch the chamber. When you are absolutely ready to proceed, click 'resume routine' in the 'PED/PLD control panel' window

- **Ablation (Step9)**

After ablation, close the substrate shutter and double click "break" on laser pad!!!

- **Removing the Sample**

Check the routine has reached step 12

Make sure all valves are closed, if not, please click 'Close Gate Valve'

Break vacuum & remove the samples & clean the substrate holder & bring it back into chamber

- **Removing the Sample from the Substrate and cleaning the silver glue.**

- **Shutdown:** Start Pumpdown → When the pressure reaches 3×10^{-5} , close gate valve → shutdown turbo without vent → close rough pump → close the Oxygen and N2 supply.

- **Record the PLD use in the log book after the routine**